This is a previous version of the article published in Desalination. 2021, 511: 115098. https://doi.org/10.1016/j.desal.2021.115098

Thermo-Economic and Environmental Optimization of a Solar-based Zero-Liquid Discharge System for Shale Gas Wastewater Desalination

Viviani C. Onishi [a, *], Mohammad H. Khoshgoftar Manesh [b, c], Raquel Salcedo-Díaz [d], Rubén Ruiz-Femenia [d], Juan A. Reyes-Labarta [d], José A. Caballero [d]

[a] School of Engineering and the Built Environment, Edinburgh Napier University, 10 Colinton Road, Edinburgh EH10 5DT, UK

[b] Energy, Environment and Biologic Research Lab (EEBRlab), Division of Thermal Sciences and Energy Systems, Department of Mechanical Engineering, Faculty of Technology & Engineering, University of Qom, Qom, Iran

[c] Center of Environmental Research, Qom, Iran

[d] Department of Chemical Engineering, University of Alicante, Ap. Correos 99, Alicante 03080, Spain

[*] ***Corresponding author at**.*

School of Engineering and the Built Environment, Edinburgh Napier University, 10 Colinton Road, Edinburgh EH10 5DT, UK. Email address: V.Onishi@napier.ac.uk (Viviani C. Onishi)

ABSTRACT

Wastewater management is one of the main hurdles encountered by the shale gas industry for boosting overall process cost-effectiveness while reducing environmental impacts. In this light, we introduce a new multi-objective model for the thermo-economic and environmental optimization of solar-based zero-liquid discharge (ZLD) desalination systems. The solar-driven ZLD system is specially developed for the desalination of high-salinity shale gas wastewaters. A decentralized system is proposed, which encompasses a solar thermal system (STS), a Rankine cycle unit, and a multiple-effect evaporation with mechanical vapor recompression (MEE-MVR) plant. The environment-friendly ZLD operation is ensured by specifying the discharge brine salinity close to salt saturation conditions. The mathematical model is formulated as a multi-objective non-linear programming (NLP) problem, aimed at the simultaneous minimization of thermo-economic and environmental objective functions. The latter objective function is quantified by the life cycle assessment (LCA)-based ReCiPe methodology. The multi-objective NLP model is implemented in GAMS software, and solved through the epsilon-constraint method. A set of trade-off Pareto-optimal solutions is presented to support decision-makers towards implementing more sustainable and cost-efficient solar-driven ZLD desalination systems. Our comprehensive energy, economic and environmental analysis reveals that the innovative system can significantly decrease costs and environmental impacts in shale gas wastewater operations.

Keywords: Optimization, shale gas wastewater, high-salinity wastewater, zero-liquid discharge (ZLD), multiple-effect evaporation (MEE), mechanical vapor recompression (MVR), renewable energy.

1. Introduction

Advances in horizontal drilling and hydraulic fracturing technologies allied to supportive policies have fueled large-scale shale gas exploration worldwide throughout the last decade. Notwithstanding, the intensification in shale gas production around the world has also fostered concerns about adverse effects on communities, public health and the environment. The environmental impacts are mainly associated with induced seismic events (NRC, 2013), greenhouse gas (GHG) emissions (Staddon and Depledge, 2015), and depletion of water resources and wastewater pollution (Prpich et al., 2016; Thomas et al., 2017). Regarding the water-related implications, the gas extraction process from shale reservoirs usually requires significant volumes of water and generates excessive amounts of high-salinity wastewater (Onishi et al., 2019). As a result, wastewater management is one of the main obstacles faced by the shale gas industry to improve overall cost-effectiveness and reduce environmental impacts (Kausley et al., 2017; Onishi et al., 2018).

In shale gas operations, thermal desalination systems based on multiple-effect evaporation with mechanical vapor recompression (MEE-MVR) provide a viable solution for the zero-liquid discharge (ZLD) treatment of high-salinity wastewaters from gas extraction. Onishi et al. (2017b) have developed a non-linear programming (NLP) model for the systematic optimization of ZLD desalination processes. The authors have carried out a thorough comparison of several system configurations –single/multiple-effect evaporation (SEE/MEE) with/without multistage compression and thermal integration– in terms of producing freshwater and achieving ZLD conditions under different inlet conditions. Their comprehensive energy and economic analysis have shown that the MEE-MVR system is the most cost-effective process for the ZLD desalination of shale gas wastewater. The authors have estimated treatment costs ranging from 6.7–10.9 US$/m^3 depending on the system configuration, while disposal costs in conventional Class II saline water injection wells are projected to be between 8–25 US$/m^3 (Acharya et al., 2011; Onishi et al., 2018). In Onishi et al. (2017a), the authors have extended their previous modelling approach to allow for the estimation of the most relevant geometrical characteristics of the desalination system during the optimization task. Their improved rigorous model has also highlighted the potential of ZLD desalination for the effective and economic shale gas wastewater treatment.

For addressing the uncertainty associated with shale gas wastewater data, Onishi et al. (2017c) have introduced a stochastic multiscenario NLP-based model for the optimal design of ZLD desalination systems. In this approach, the authors have considered both wastewater salinity and flowrate as uncertain design parameters to enhance system flexibility and reliability. Thus, the latter uncertain parameters have been modelled as a set of correlated feeding water scenarios with a given probability of occurrence. The authors have presented cumulative probability curves to appraise the economic risk linked to the uncertain space for distinct standard deviations of expected mean values. Their results reveal that the proposed stochastic multiscenario approach leads to improved thermo-economic performance solutions in comparison to previous deterministic models.

Although aforementioned studies have highlighted the feasibility of zero-liquid discharge MEE-MVR desalination systems for reducing wastewater impacts while improving water resources, their practical implementation is still restricted by their intensive energy consumption and associated pollutant carbon emissions. For instance, the SEE/MEE-MVR technologies for ZLD desalination developed in Onishi et al. (2017b) have presented specific energy consumption ranging from 28–50.5 kWh$_e$ per cubic meter of produced freshwater. According to the US Energy Information Administration (EIA, 2016), about 939 g/kWh$_e$ of CO_2 are generated to produce electricity from burning coal. Under the latter assumption, the referred SEE/MEE-MVR systems operating at ZLD conditions would yield to ~26–47 kg of CO_2 per cubic meter of produced freshwater (Onishi et al., 2018; Onishi et al., 2017b). These results emphasize the need for developing more sustainable alternatives for ZLD desalination systems, particularly involving the integration of renewable energy resources.

The integration of solar thermal energy to power desalination systems has attracted increased interest from the literature over the past few years. Into this framework, Pouyfaucon and García-Rodríguez (2018) have studied different solar thermal-powered desalination technologies to identify main issues for improving market opportunities. The authors have presented a thorough performance and economic analysis of distinct membrane distillation (MD) and reverse osmosis (RO)-based desalination systems assisted by solar photovoltaic and solar thermal power plants. Their analysis has included parabolic trough collectors, linear Fresnel concentrators, and dish concentrators. Moore et al. (2018) have examined the coupling of thermal solar thermal collectors to sweeping-gas MD systems via economic optimization. Karanikola et al. (2019) have also provided an economic performance evaluation of MD desalination system driven by solar photovoltaic and solar thermal collectors. Zheng and Hatzell (2020) have developed a techno-economic model to evaluate the viability of combining solar collectors with multistage flash distillation (MSF) systems. Their model accounts for several factors such as system lifetime and scale, performance parameters of different system units, and payback period, aimed at surpassing geographic and technical constraints.

Aboelmaaref et al. (2020) have presented a comprehensive review on concentrated solar power (CSP) desalination technologies. The authors have paid particular attention on the thermodynamic and economic analysis of desalination systems driven by parabolic trough collectors and parabolic dish CSP technologies. Ghenai et al. (2021) have proposed an optimization approach based on response surface for improving hybrid multi-effect distillation (MED) and adsorption desalination (AD) systems powered by solar thermal energy. Their optimization method, along with performance analysis and parametric study, are used to identify the optimal operating conditions to increase the freshwater production while reducing energy consumption. Even though previous studies have presented insightful results on the integration of solar thermal technologies to desalination plants, none of them have considered ZLD processes. To tackle this issue, Najaf et al. (2019) have performed a thermo-economic evaluation of a ZLD desalination plant equipped with parabolic trough solar collectors. Their simulation model approach is focused on an industrial wastewater treatment plant composed of a brine concentrator and a forced-circulation crystallizer. However, their approach disregards energy intensive high-salinity applications, as well as the assessment of environmental impacts of the process.

To overcome shortcomings in preceding research, we introduce a new multi-objective modelling approach for the thermo-economic and environmental optimization of solar-driven ZLD desalination systems. The mathematical model is developed upon a multistage superstructure, which includes a solar thermal system (STS), a Rankine cycle (RC) unit, and a MEE-MVR desalination plant. The proposed desalination process is particularly applied for treating high-salinity shale gas wastewaters. In this system, the ZLD operation is ensured by a design constraint that specifies the discharge brine salinity close to salt saturation conditions. Also, the STS is designed to operate in different time periods to account for the intermittency in daily solar irradiance throughout the year. The model is formulated as a multi-objective NLP problem, which is implemented in GAMS software and solved via the epsilon-constraint method to minimize both thermo-economic and environmental objective functions. The environmental performance is evaluated by the LCA-based ReCiPe methodology. Our methodology allows obtaining a set of alternative Pareto-optimal solutions to support decision-makers towards the implementation of more environment-friendly and cost-effective solar-driven ZLD desalination systems.

The rest of this paper is organized as follows. In **Section 2**, we briefly introduce the problem statement of multi-objective optimization of solar-driven

ZLD desalination systems. The process description of the MEE-MVR desalination plant, and RC and STS units are presented in **Section 3**. In **Section 4**, we developed the multi-objective modelling approach. The illustrative case study used to assess the applicability of the proposed model is described in **Section 5**, while the main results obtained are discussed in **Section 6**. Finally, we summarize the main conclusions in **Section 7**.

2. Problem Statement

The multi-objective optimization problem can be formally stated as follows. We are given the inlet feed water (*i.e.*, high-salinity shale gas wastewater) conditions (which include temperature, salinity, and mass flowrate), and the ZLD target state. The technical characteristics of the MEE-MVR system, Rankine cycle units, and solar parabolic trough collectors are also known, along with weather conditions, economic, and environmental impact data. Utilities (electricity, natural gas, and cooling water) are provided with their corresponding prices and environmental data. The main goal is to obtain an optimal design and operating conditions for the solar-based ZLD desalination system that simultaneously enhance its thermal-economic and environmental performances. To do so, a multi-objective NLP-based model is developed and solved via the epsilon-constraint method, through the minimization of the economic and environmental objective functions. In this approach, the solar thermal system (STS) should follow a multi-period operation to account for the different weather conditions throughout the year. In addition, the ZLD operation is ensured by adding a design constraint that sets the discharge salinity close to the salt saturation condition. The process description is presented as follows.

3. Process Description

For our analysis, we consider an integrated system composed of a MEE-MVR desalination plant, STS, and Rankine cycle unit. The schematic diagram for the solar-based ZLD desalination system is displayed in **Fig. 1**.

3.1. MEE-MVR Desalination System

The zero-discharge MEE-MVR desalination plant encompasses a multiple-effect horizontal-tube evaporator, which is coupled to intermediate flashing tanks for enhancing energy recovery efficiency. In the system, a feeding-distillate preheater is also used to further increase the thermal integration, whilst the vapor produced by flashing and evaporation processes are managed by a mechanical compressor. Further details on the design and operation of MEE-MVR desalination systems are presented in our previous studies (Onishi et al., 2017a, 2017b, 2017c).

3.2. Rankine Cycle Unit

The Rankine cycle unit embraces a steam turbine, a condenser, a pump, and a boiler. The Rankine cycle unit is used to convert the solar energy from the STS into the electric power required by the mechanical vapor compressor in the MEE-MVR desalination plant. In this cycle, the subcooled water (RC working fluid) exchanges heat with the thermal solar fluid of the STS in the boiler to produce superheated vapor. Then, the superheated vapor is used to produce electricity by passing through the turbine generator. The humid vapor from the turbine exchanges heat with cooling water in the condenser before being pumped back to the boiler to restart the cycle.

3.3. Solar Thermal System

The STS is comprised by a solar field of parabolic trough collectors, in which the solar thermal energy is transferred to the thermal operating fluid (*i.e.*, mineral oil).

A backup natural gas-fired heater (GFH) is used to meet the energy shortages that could result from the daily solar intermittency. The GFH ensures the constant energy supply to the MEE-MVR desalination plant, by keeping the thermal operating fluid of the STS at constant temperature.

4. Multi-objective Optimization Model

The multi-objective mathematical model for the optimal design and operation of solar-driven ZLD thermal desalination systems is developed through an NLP-based formulation. The optimization approach encompasses the thermodynamic modelling equations of the MEE-MVR desalination plant, steam Rankine cycle, solar thermal collectors' system, and economic and environmental objective functions. The model is built upon the general superstructure as shown in **Fig. 1**. The multi-objective optimization model is presented in the following sections, in which the solar-driven MEE-MVR superstructure is generated according to the subsequent steps.

4.1. Modelling of the Thermal Desalination System

The mathematical programming model for optimizing the MEE-MVR desalination plant comprises energy and mass balances, temperature and pressure feasibility restrictions, along with the ZLD design constraint. The mathematical formulation is based on our previous studies concerning the design and optimization of MEE-MVR desalination systems presented in Onishi et al. (2017a, 2017b, 2017c). In this study, we take into consideration the following assumptions to simplify the model formulation:

(i) Steady-state operation.

(ii) Thermal losses in system units are negligible.

(iii) Vapor streams in evaporator effects are modelled as an ideal gas.

(iv) Pressure drops in system units are negligible.

(v) The non-equilibrium allowance (NEA) is negligible.

(vi) The mechanical compressor is isentropic.

(vii) The starter power of the mechanical compressor is negligible.

(viii) Capital costs of mixers are negligible.

The following index set is required for better developing of the NLP-based model:

$$I = \{ i \,/\, i = 1, 2, ..., I \ \ is\ an\ evaporator\ effect \}$$

4.1.1. Multiple-effect Evaporator Unit

The mass balances in the evaporator effect i can be expressed as follows.

$$\begin{cases} \dot{m}_{i+1}^{brine} = \dot{m}_i^{vapor} + \dot{m}_i^{brine} \\ \dot{m}_i^{brine} \cdot S_i^{brine} = \dot{m}_{i+1}^{brine} \cdot S_{i+1}^{brine} \end{cases} \quad \forall\ 1 \le i \le I-1 \tag{1}$$

$$\begin{cases} \dot{m}_i^{feed} = \dot{m}_i^{vapor} + \dot{m}_i^{brine} \\ \dot{m}_i^{feed} \cdot S_{in}^{feed\_water} = \dot{m}_i^{brine} \cdot S_i^{brine} \end{cases} \quad \forall\ i = I \tag{2}$$

It should be noted that the system operates under a backward feeding configuration. As a result, the brine salinity in the first evaporation effect $i=1$ should match the ZLD design constraint (to ensure the ZLD operation), while salinity of the feed water is considered in the last effect $i=I$. For evaporation effects in between, that is $1 < i \le I-1$, brine is added as feeding stream.

The global energy balances in evaporator effects $i \in I$ are given by **Eq. (3)** and **Eq. (4)**.

$$Q_i + \dot{m}_{i+1}^{brine} \cdot H_{i+1}^{brine} = \dot{m}_i^{brine} \cdot H_i^{brine} + \dot{m}_i^{vapor} \cdot H_i^{vapor} \quad \forall\ i < I \tag{3}$$

$$Q_i + m_{in}^{feed} \cdot H_i^{feed} = \dot{m}_i^{brine} \cdot H_i^{brine} + \dot{m}_i^{vapor} \cdot H_i^{vapor} \quad \forall\ i = I \tag{4}$$

In which, Q_i indicates the heat flow supplied to system boundary by the condensed vapor. The specific enthalpies of brine, feed water and boiling vapor are estimated via correlations as presented in the **Appendix**. Note that brine and vapor are both at the same boiling temperature $T_i^{boiling}$ in the effect $i \in I$. The latter is evaluated by considering the boiling point elevation (BPE) over the ideal temperature in the evaporation effect i as follows.

$$T_i^{boiling} = T_i^{ideal} + BPE_i \quad \forall\ i \in I \tag{5}$$

In which, BPE_i and ideal temperature T_i^{ideal} in the effect $i \in I$ are estimated by the correlations provided in the **Appendix**.

The energy requirements in evaporator effects $i \in I$ are given by the following equations.

$$Q_i = \dot{m}^{sup} \cdot Cp_i^{vapor} \cdot \left(T^{sup} - T_i^{condensate}\right) + \dot{m}^{sup} \cdot \left(H_i^{cv} - H_i^{condensate}\right) + Q^{external} \quad \forall\ i = 1 \tag{6}$$

$$Q_i = \lambda_i \cdot \left(\dot{m}_{i-1}^{vapor} + \dot{m}_{c_{i-1}}^{vapor}\right) \quad \forall\ i > 1 \tag{7}$$

In the evaporator effect $i = 1$, energy requirements embrace the sensible heat needed to achieve the outlet temperature of the condensate, and the latent heat of condensation of the superheated vapor. In other evaporator effects, the energy requirements are calculated by the latent heat of vaporization added to the effect by the boiling vapor and flashed off condensate vapor. In **Eq. (6)**, $Q^{external}$ represents the energy from a steam external source that is used to avoid equipment oversizing. This energy amount is estimated as follows.

$$Q^{external} = \dot{m}^{steam} \cdot Cp^{vapor} \cdot \left(T^{steam} - T_i^{condensate}\right) + \dot{m}^{steam} \cdot \left(H_i^{cv} - H_i^{condensate}\right) \quad \forall\ i = 1 \tag{8}$$

In **Eq. (6)** and **Eq. (8)**, the specific enthalpies for vapor H_i^{cv} and condensate $H_i^{condensate}$ phases are given by the correlations presented in the **Appendix**. Note that the condensate temperature $T_i^{condensate}$ in effects $i \in I$ is obtained by considering the outlet vapor pressure of the mechanical compressor in the Antoine Equation (please see the **Appendix**).

In **Eq. (6)**, $\dot{m}^{sup}$ is the superheated mass flowrate as given by the following equation.

$$\dot{m}^{sup} = \dot{m}_i^{vapor} + \dot{m}_{c_i}^{vapor} \quad \forall\ i = I \tag{9}$$

In which, $\dot{m}_{c_i}^{vapor}$ and $\dot{m}_i^{vapor}$ are mass flowrates of the flashed off and boiling vapor from the condensate in evaporator effects $i \in I$, correspondingly.

The total heat transfer area of the evaporator unit of is obtained by the sum of the corresponding areas of each effect as shown in the **Eq. (10)**.

$$A^{evaporator} = \sum_{i=1}^{I} A_i \quad \forall\ i \in I \tag{10}$$

In evaporator effect $i = 1$, the heat transfer area should correspond to the sum of the areas related to the latent and sensible heat transfer:

$$A_i = \begin{bmatrix} \dot{m}^{sup} \cdot Cp_i^{vapor} \cdot \left(T^{sup} - T_i^{condensate}\right) \Big/ \left(U^S \cdot LMTD_i\right) + \\ \dot{m}^{sup} \cdot \left(H_i^{cv} - H_i^{condensate}\right) \Big/ U_i \cdot \left(T_i^{condensate} - T_i^{boiling}\right) \end{bmatrix} \quad \forall\ i = 1 \tag{11}$$

For remaining evaporator effects, the following equation is used to estimate the heat transfer area:

$$A_i = Q_i \Big/ \left(U_i \cdot LMTD_i\right) \quad \forall\ i > 1 \tag{12}$$

In which, U_i is the overall heat transfer coefficient that is given by the following correlation (Al-Mutaz and Wazeer, 2014).

$$U_i = 0.001 \cdot \begin{bmatrix} 1939.4 + 1.40562 \cdot T_i^{boiling} - 0.00207525 \cdot \left(T_i^{boiling}\right)^2 + \\ 0.0023186 \cdot \left(T_i^{boiling}\right)^3 \end{bmatrix} \quad \forall\ i \in I \qquad (13)$$

In **Eq. (11)** and **Eq. (12)**, $LMTD_i$ indicates the log mean temperature difference in evaporator effect $i \in I$. The latter is estimated by using the Chen's approximation (Chen, 1987) for avoiding numerical difficulties related to the temperature differences.

$$LMTD_i = \left[0.5 \cdot \left(\theta_{1i} \cdot \theta_{2i}\right) \cdot \left(\theta_{1i} + \theta_{2i}\right)\right]^{\frac{1}{3}} \quad \forall\ i \in I \qquad (14)$$

In which,

$$\theta_{1i} = \begin{cases} T^{\sup} - T_i^{boiling} & \forall\ i = 1 \\ T_i^{sat} - T_i^{boiling} & \forall\ i > 1 \end{cases} \qquad \theta_{2i} = \begin{cases} T_i^{condensate} - T_{i+1}^{boiling} & \forall\ i = 1 \\ T_i^{sat} - T_{i+1}^{boiling} & \forall\ 1 < i < I \\ T_i^{sat} - T_i^{feed} & \forall\ i = I \end{cases} \qquad (15)$$

The following constraint is used to ensure the pressure feasibility in evaporation effects $i \in I$.

$$P_i^{vapor} \geq P_{i+1}^{vapor} + \Delta P_{\min} \quad \forall\ i < I \qquad (16)$$

In which the vapor pressure P_i^{vapor} should equal the pressure of saturated vapor from subsequent effect to avoid operating instabilities:

$$P_i^{vapor} = P_{i+1}^{sat} \quad \forall\ i < I \qquad (17)$$

Finally, the following temperature constraints are considered to avoid temperature crossovers in evaporator effects $i \in I$.

$$\begin{cases} T^{sup} \geq T_i^{condensate} + \Delta T_{\min}^1 & \forall\ i = 1 \\ T_{i-1}^{boiling} \geq T_i^{condensate} + \Delta T_{\min}^1 & \forall\ i > 1 \\ T_i^{boiling} \geq T_{i+1}^{boiling} + \Delta T_{\min}^2 & \forall\ i < I \\ T_i^{boiling} \geq T_i^{feed} + \Delta T_{\min}^2 & \forall\ i = I \\ T_i^{condensate} \geq T_{i+1}^{boiling} + \Delta T_{\min}^3 & \forall\ i < I \\ T_i^{condensate} \geq T_i^{feed} + \Delta T_{\min}^3 & \forall\ i = I \\ T_i^{condensate} \geq T_i^{boiling} + \Delta T_{\min}^4 & \forall\ i \in I \\ T_i^{sat} \geq T_i^{boiling} + \Delta T_{\min}^4 & \forall\ i \in I \end{cases} \tag{18}$$

4.1.2. Flashing Tanks

The mass balances in the flashing unit of the evaporator effect i can be expressed as follows.

$$\dot{m}^{sup} = \dot{m}_{c_i}^{vapor} + \dot{m}_{c_i}^{liquid} \qquad \forall\ i = 1 \tag{19}$$

$$\dot{m}_{i-1}^{vapor} + \dot{m}_{c_{i-1}}^{vapor} + \dot{m}_{c_{i-1}}^{liquid} = \dot{m}_{c_i}^{vapor} + \dot{m}_{c_i}^{liquid} \qquad \forall\ i > 1 \tag{20}$$

In which, $\dot{m}_{c_i}^{vapor}$ and $\dot{m}_{c_i}^{liquid}$ represent the mass flowrates of vapor and liquid phases of the flashed off condensate in the effect $i \in I$, respectively.

The energy balances in the flashing unit of the evaporator effect i are given by the following equations.

$$\dot{m}^{sup} \cdot H_i^{condensate} = \dot{m}_{c_i}^{vapor} \cdot H_{c_i}^{vapor} + \dot{m}_{c_i}^{liquid} \cdot H_{c_i}^{liquid} \qquad \forall\ i = 1 \tag{21}$$

$$\left(\dot{m}_{i-1}^{vapor} + \dot{m}_{c_{i-1}}^{vapor}\right) \cdot H_i^{condensate} + \dot{m}_{c_{i-1}}^{liquid} \cdot H_{c_{i-1}}^{liquid} = \dot{m}_{c_i}^{vapor} \cdot H_{c_i}^{vapor} + \dot{m}_{c_i}^{liquid} \cdot H_{c_i}^{liquid} \qquad \forall\ i > 1 \tag{22}$$

In which, $H_{c_i}^{vapor}$ and $H_{c_i}^{liquid}$ are the specific enthalpies for vapor and liquid phases of the flashed off condensate in the effect $i \in I$, respectively. They are estimated at the ideal temperature via correlations as presented in the **Appendix**.

The volume of the flashing unit of the evaporator effect i is determined by **Eq. (23)** and **Eq. (24)**.

$$V_i^{flash} = \left(\dot{m}^{sup} \cdot rt\right) \Big/ \rho_i \qquad \forall\ i = 1 \tag{23}$$

$$V_i^{flash} = \left(\dot{m}_{i-1}^{vapor} + \dot{m}_{c_{i-1}}^{liquid}\right) \cdot rt \Big/ \rho_i \qquad \forall\ i > 1 \tag{24}$$

In which, rt and ρ_i indicate the time of retention in the flashing tank and condensate density, correspondingly. In this study, we consider a retention time of 5 min.

4.1.3. Mechanical Vapor Compressor

The outlet isentropic temperature of the mechanical vapor compressor is given as follows.

$$T^{is} = \left(T_i^{mix} + 273.15\right) \cdot \left(P^{sup} \Big/ P_i^{vapor}\right)^{\frac{\gamma-1}{\gamma}} - 273.15 \qquad \forall\ i = I \tag{25}$$

In **Eq. (25)**, T_i^{mix} indicates the temperature of mixture obtained from an energy balance of the mixer in the last evaporator effect $i = I$. P^{sup} is the pressure of superheated vapor, which is limited by the maximum compression ratio $CR_{\max}$ as expressed by **Eq. (26)**.

$$P^{sup} \le CR_{\max} \cdot P_i^{vapor} \qquad \forall\ i = I \tag{26}$$

The temperature of the superheated vapor from the mechanical vapor compressor is estimated by **Eq. (27)**.

$$T^{sup} = T_i^{mix} + \frac{1}{\eta^{IS}} \cdot \left(T^{IS} - T_i^{mix}\right) \qquad \forall\ i = I \tag{27}$$

In which, η^{IS} represents the isentropic efficiency of the compressor.

The compressor mechanical power is given by the following equation.

$$W^{compressor} = \dot{m}^{sup} \cdot \left(H^{sup} - H_i^{vapor} \right) \qquad \forall\ i = I \tag{28}$$

In which, H^{sup} and H_i^{vapor} are specific enthalpies of vapor evaluated at superheated and mixture temperatures, respectively. The correlations of vapor specific enthalpies are shown in the **Appendix**. The following constraints on the superheated temperature and pressure are used to guarantee the proper operation of the compressor.

$$T^{sup} \geq T_i^{mix} \qquad \forall\ i = I \tag{29}$$

$$P^{sup} \geq P_i^{vapor} \qquad \forall\ i = I \tag{30}$$

4.1.4. Feeding Preheater

The global energy balance in the feeding preheater unit is stated as follows.

$$\dot{m}_{c_i}^{liquid} \cdot Cp_i^{condensate} \cdot \left(T_i^{ideal} - T_{out}^{freshwater} \right) = \dot{m}_{in}^{feed} \cdot Cp_{in}^{feed} \cdot \left(T_i^{feed} - T_{in}^{feed} \right) \quad \forall\ i = I \tag{31}$$

In which, T_{in}^{feed} and $T_{out}^{freshwater}$ are temperatures of the feed water and produced freshwater by the system, correspondingly. The specific heats of the condensate and feed water are obtained via correlations as presented in the **Appendix**.

The heat transfer area of the feeding preheater is given by **Eq. (32)**.

$$A^{preheater} = \dot{m}_{c_i}^{liquid} \cdot Cp_i^{condensate} \cdot \left(T_i^{ideal} - T_{out}^{freshwater} \right) \Big/ \left(U \cdot LMTD \right) \qquad \forall\ i = I \tag{32}$$

In which, U represents the overall heat transfer coefficient at T_i^{ideal} as estimated by **Eq. (13)**. The logarithmic mean temperature difference $LMTD$ is obtained by **Eq. (14)**. In this case, the temperature differences are stated as follows.

$$\begin{cases} \theta_1 = T_i^{ideal} - T_i^{feed} & \forall \ i = I \\ \theta_2 = T_{out}^{freshwater} - T_{in}^{feed} \end{cases} \tag{33}$$

4.1.5. Zero-Liquid Discharge Specification

The zero-liquid discharge operation of the thermal desalination system is ensured by the following design constraint.

$$S_i^{brine} \geq S^{design} \qquad \forall \ i = 1 \tag{34}$$

4.2. Modelling of the Steam Rankine Cycle

The thermal efficiency of the steam Rankine cycle is given by the following equation.

$$\eta^{RC} = \frac{W^{RC}}{Q^{Boiler}} \tag{35}$$

In which, W^{RC} represents the net power of the Rankine cycle, while Q^{Boiler} is the thermal power of the boiler. The following inequality constraint is required to couple the steam Rankine cycle to the MEE-MVR desalination system.

$$W^{RC} \geq W^{compressor} \tag{36}$$

In which, **Eq. (36)** is used to ensure that net power provided by the Rankine cycle is higher or equal to the power needed to drive the compressor in the desalination system. The net power of the Rankine cycle is given as follows.

$$W^{RC} = W^{turbine} - W^{RC\_pump} \tag{37}$$

In which, $W^{turbine}$ and W^{RC_pump} represent the mechanical power produced by the steam turbine and consumed by the pump in the Rankine cycle, respectively. The modelling equations of the steam turbine, pump, and condenser of the steam Rankine cycle are presented in the next sections.

4.2.1. Steam Turbine

The mechanical power produced by the steam turbine is given by the following equation.

$$W^{turbine} = \dot{m}^{RC} \cdot \left(H_{in}^{turbine} - H_{out}^{turbine} \right) \tag{38}$$

In **Eq. (38)**, $\dot{m}^{RC}$ indicates the mass flowrate of the working fluid (water) in the Rankine cycle, which is constant throughout the cycle. $H_{in}^{turbine}$ and $H_{out}^{turbine}$ are the specific enthalpies of the working fluid at the inlet and outlet of the turbine, respectively. The specific enthalpy of vapor at the turbine outlet $H_{out}^{turbine}$ is estimated from the definition of isentropic efficiency η^{IS} as follows.

$$H_{out}^{turbine} = H_{in}^{turbine} - \eta^{IS} \cdot \left(H_{in}^{turbine} - H_{out}^{IS} \right) \tag{39}$$

The isentropic enthalpy of the humid vapor at the turbine outlet is defined as follows.

$$H_{out}^{IS} = H_{out}^{L} - x^{IS} \cdot \left(H_{out}^{V} - H_{out}^{L} \right) \tag{40}$$

The vapor quality in the isentropic expansion process, and the actual vapor quality at the turbine outlet are given the following expressions.

$$x^{IS} = \frac{s_{out}^{turbine} - s_{out}^{L}}{s_{out}^{V} - s_{out}^{L}} \tag{41}$$

$$x_{out}^{turbine} = \frac{H_{out}^{turbine} - H_{out}^{L}}{H_{out}^{V} - H_{out}^{L}} \tag{42}$$

The specific enthalpies and entropies of liquid and vapor states at the turbine outlet are estimated by the following correlations (Lemmon et al., 1980; National Institute of Standards, 2011).

$$H_{out}^{L} = a_{hL} + b_{hL} \cdot T^{sat} + c_{hL} \cdot \left(T^{sat}\right)^{2} + d_{hL} \cdot \left(T^{sat}\right)^{3} + e_{hL} \cdot \left(T^{sat}\right)^{4} + f_{hL} \cdot \left(T^{sat}\right)^{5} \tag{43}$$

$$H_{out}^{V} = a_{hV} + b_{hV} \cdot T^{sat} + c_{hV} \cdot \left(T^{sat}\right)^{2} + d_{hV} \cdot \left(T^{sat}\right)^{3} + e_{hV} \cdot \left(T^{sat}\right)^{4} + f_{hV} \cdot \left(T^{sat}\right)^{5} \tag{44}$$

$$s_{out}^{L} = a_{sL} + b_{sL} \cdot T^{sat} + c_{sL} \cdot \left(T^{sat}\right)^{2} + d_{sL} \cdot \left(T^{sat}\right)^{3} + e_{sL} \cdot \left(T^{sat}\right)^{4} + f_{sL} \cdot \left(T^{sat}\right)^{5} \tag{45}$$

$$s_{out}^{V} = a_{sV} + b_{sV} \cdot T^{sat} + c_{sV} \cdot \left(T^{sat}\right)^{2} + d_{sV} \cdot \left(T^{sat}\right)^{3} + e_{sV} \cdot \left(T^{sat}\right)^{4} + f_{sV} \cdot \left(T^{sat}\right)^{5} \tag{46}$$

The following inequality constraints are used to guarantee the temperature and pressure feasibility in the steam turbine.

$$\begin{cases} T_{out}^{turbine} \le T_{in}^{turbine} \\ T_{in}^{turbine} \ge T_{in}^{sat} \\ P_{out}^{sat} \le P_{in}^{sat} \end{cases} \tag{47}$$

The pressure of vapor in saturation conditions is obtained from the modified version of the Antoine equation as available in the process simulator Aspen HYSYS.

$$P^{sat} = \exp\left(A + \frac{B}{C + T^{sat}} + D \cdot \ln\left(T^{sat}\right) + E \cdot \left(T^{sat}\right)^{F} \right) \tag{48}$$

4.2.2. Rankine Cycle Pump

The power consumed by the pump in the Rankine cycle is estimated as follows.

$$W^{RC\_pump} = \frac{\dot{m}^{RC} \cdot v \cdot \left(P_{in}^{sat} - P_{out}^{sat}\right)}{\eta^{RC\_pump}} \tag{49}$$

In which, v represents the specific volume of liquid water, while η^{RC_pump} indicates the RC pump efficiency. The specific enthalpy of the working fluid at the pump outlet is obtained by the following equation.

$$H_{out}^{RC\_pump} = H_{in}^{RC\_pump} + v \cdot \left(P_{in}^{sat} - P_{out}^{sat}\right) \tag{50}$$

Note that the properties at the inlet of the pump should correspond to those at the condenser outlet in the Rankine cycle. Hence, $H_{in}^{RC\_pump} = H_{out}^{condenser}$.

4.2.3. Condenser

The thermal power of the condenser in the Rankine cycle is given as follows.

$$Q^{condenser} = \dot{m}^{RC} \cdot \left(H_{in}^{condenser} - H_{out}^{condenser}\right) \tag{51}$$

In which, $H_{in}^{condenser}$ and $H_{out}^{condenser}$ are the specific enthalpies of the working fluid at the inlet and outlet of the condenser, respectively. Note that the properties at the inlet of the condenser should correspond to those at the turbine outlet. Hence, $H_{in}^{condenser} = H_{out}^{turbine}$.

The heat transfer area of the condensed can be obtained by the following equation.

$$A^{condenser} = \frac{Q^{condenser}}{U^{condenser} \cdot LMTD^{condenser}} \tag{52}$$

In which, $U^{condenser}$ indicates the heat transfer coefficient. The logarithmic mean temperature difference $LMTD^{condenser}$ is obtained through the Chen's approximation as given by **Eq. (14)** (Chen, 1987). In this case, the temperature differences are stated as follows.

$$\begin{cases} \theta_1 = T_{in}^{condenser} - T_{out} \\ \theta_2 = T_{out}^{condenser} - T_{in} \end{cases} \tag{53}$$

In which,

$$\begin{cases} T_{in}^{condenser} \geq T_{out} + \Delta T_{\min} \\ T_{out}^{condenser} \geq T_{in} + \Delta T_{\min} \end{cases} \tag{54}$$

The thermal power required by the Rankine cycle to generate super-heated steam in the boiler outlet is provided by heat exchanges with the solar thermal system. The modelling equations for the solar thermal system are presented as follows.

4.3. Modelling of the Solar Thermal System

The solar thermal system is designed to operate in different time periods, which account for the daily solar radiation flux (irradiance) throughout the year. Thus, the following index set is needed to develop the multi-period model for the solar thermal system design.

$$\mathrm{T} = \left\{ t / t = 1, 2, ..., \mathrm{T} \;\; \textit{is a time period} \right\}$$

The heat demands of the boiler are provided by the solar collectors' field and a backup gas-fired heater. Therefore, the global energy balance in the solar thermal system is expressed as follows.

$$Q_t^{boiler} = Q_t^{SC} + Q_t^{GFH} \qquad \forall \; t \in \mathrm{T} \tag{55}$$

In which, Q_t^{boiler}, Q_t^{SC} and Q_t^{GFH} refer to the thermal power of the boiler, solar collectors field, and gas-fired heater in the time period $t \in \mathrm{T}$, respectively.

The mass balances at each node of the solar thermal system are given by the following formulation.

$$\begin{cases} \dot{m}_{\text{out},t}^{boiler} = \dot{m}_{\text{in},t}^{SC} + \dot{m}_{\text{in},t}^{GFH} \\ \dot{m}_{\text{in},t}^{boiler} = \dot{m}_{\text{out},t}^{SC} + \dot{m}_{\text{out},t}^{GFH} \\ \dot{m}_{\text{in},t}^{boiler} = \dot{m}_{\text{out},t}^{boiler} \\ \dot{m}_{\text{in},t}^{SC} = \dot{m}_{\text{out},t}^{SC} \\ \dot{m}_{\text{in},t}^{GFH} = \dot{m}_{\text{out},t}^{GFH} \end{cases} \qquad \forall \; t \in \mathrm{T} \tag{56}$$

The energy balances at each node of the solar thermal system are given by the following formulation.

$$\begin{cases} \dot{m}_{\text{out},t}^{boiler} \cdot H_{\text{out},t}^{boiler} = \dot{m}_{\text{in},t}^{SC} \cdot H_{\text{in},t}^{SC} + \dot{m}_{\text{in},t}^{GFH} \cdot H_{\text{in},t}^{GFH} \\ \dot{m}_{\text{in},t}^{boiler} \cdot H_{\text{in},t}^{boiler} = \dot{m}_{\text{out},t}^{SC} \cdot H_{\text{out},t}^{SC} + \dot{m}_{\text{out},t}^{GFH} \cdot H_{\text{out},t}^{GFH} \\ H_{\text{out},t}^{boiler} = H_{\text{in},t}^{SC} \\ H_{\text{out},t}^{boiler} = H_{\text{in},t}^{GFH} \end{cases} \qquad \forall \; t \in \mathrm{T} \tag{57}$$

In which the specific enthalpies of the heating fluid (oil Therminol 72) at the inlet and outlet of each solar thermal system equipment are estimated as follows.

$$H_t = Cp^{hf} \cdot T_t \qquad \forall\, t \in \mathrm{T} \tag{58}$$

In which, Cp^{hf} indicates the specific heat, and T_t the temperature of the heating fluid in the time period $t \in \mathrm{T}$.

4.3.1. Solar Thermal Collectors

The thermal power produced by the solar collectors' field in the time period $t \in \mathrm{T}$ is given by **Eq. (59)**.

$$Q_t^{SC} = \dot{m}_{\mathrm{in},t}^{SC} \cdot \left(H_{\mathrm{out},t}^{SC} - H_{\mathrm{in},t}^{SC} \right) \qquad \forall\, t \in \mathrm{T} \tag{59}$$

The total area of the solar parabolic trough collectors is estimated as follows.

$$A^{SC} \geq \frac{Q_t^{SC}}{G_t \cdot \eta^{SC}} \qquad \forall\, t \in \mathrm{T} \tag{60}$$

In **Eq. (60)**, G_t is the daily solar radiation flux (irradiance) in the time period $t \in \mathrm{T}$. Also, η^{SC} is the thermal efficiency of the medium-high temperature solar parabolic trough collectors as given by the following expression (Salcedo et al., 2012).

$$\eta^{SC} = \eta_0 - a_1 \cdot \left(T_t^{avg} - T_t^{amb} \right) - a_2 \cdot \left(\frac{T_t^{avg} - T_t^{amb}}{G_t} \right) - a_3 \cdot \left(\frac{T_t^{avg} - T_t^{amb}}{G_t} \right)^2 \qquad \forall\, t \in \mathrm{T} \tag{61}$$

In which, η_0 is the collector optical efficiency, while a_1, a_2, and a_3 are coefficients. T_t^{amb} and T_t^{avg} are the ambient and average temperatures in the time period $t \in \mathrm{T}$, respectively. The average temperature of the solar collectors is calculated as follows.

$$T_t^{avg} = 0.5 \cdot \left(T_{\mathrm{in},t}^{SC} + T_{\mathrm{out},t}^{SC} \right) \qquad \forall\ t \in \mathrm{T} \tag{62}$$

4.3.2. Gas-Fired Heater

The thermal power produced by the natural gas-fired heater in the time period $t \in \mathrm{T}$ is estimated as follows.

$$Q_t^{GFH} = \dot{m}_t^{ng} \cdot LHV \cdot \eta^{GFH} \qquad \forall\ t \in \mathrm{T} \tag{63}$$

In which, $\dot{m}_t^{ng}$ and LHV indicate the mass flowrate and lower heating value of natural gas, respectively. η^{GFH} is the thermal efficiency of the natural gas heater.

4.3.3. Boiler

The thermal power of the boiler in the time period $t \in \mathrm{T}$ is given as follows.

$$Q_t^{boiler} = \dot{m}_{\mathrm{in},t}^{boiler} \cdot \left(H_{\mathrm{in},t}^{boiler} - H_{\mathrm{out},t}^{boiler} \right) \qquad \forall\ t \in \mathrm{T} \tag{64}$$

The heat transfer area of the boiler can be estimated by the following equation.

$$A^{boiler} = \frac{Q_t^{boiler}}{U^{boiler} \cdot LMTD_t^{boiler}} \tag{65}$$

In which, U^{boiler} indicates the heat transfer coefficient. The logarithmic mean temperature difference $LMTD_t^{boiler}$ in the time period $t \in \mathrm{T}$ is obtained through the Chen's approximation as given by **Eq. (14)** (Chen, 1987). In this case, the temperature differences are stated as follows.

$$\begin{cases} \theta_1 = T_{\mathrm{in},t}^{boiler} - T_{in}^{turbine} \\ \theta_2 = T_{\mathrm{out},t}^{boiler} - T_{out}^{RC\_pump} \end{cases} \tag{66}$$

In which,

$$\begin{cases} T_{\mathrm{in},t}^{boiler} \ge T_{in}^{turbine} + \Delta T_{\min} \\ T_{\mathrm{out},t}^{boiler} \ge T_{out}^{RC\_pump} + \Delta T_{\min} \end{cases} \quad (67)$$

4.4. Economic and Environmental Objective Functions

As mentioned before, the multi-objective NLP-based model is optimized via the simultaneous minimization of economic and environmental objective functions. These objective functions are presented in the following sections.

4.4.1. Economic Performance Evaluation

The economic objective function corresponds to the minimization of the total annualized cost of the solar-assisted MEE-MVR system. The total annualized cost (TAC) is composed of the total capital investment ($CAPEX$) in all system devices, and total operating and maintenance expenses ($OPEX$) as stated as follows.

$$TAC = CAPEX + OPEX \quad (68)$$

The total capital investment comprises the costs of all equipment units from the MEE-MVR desalination system, steam Rankine cycle, and solar thermal system:

$$CAPEX = CAPEX^{MEE-MVR} + CAPEX^{RC} + CAPEX^{STS} \quad (69)$$

In which,

$$CAPEX^{MEE-MVR} = fac \cdot \left(\frac{CEPCI^{2019}}{CEPCI^{2003}} \right) \cdot \left[\begin{array}{l} \left(C_{PO} \cdot F_{BM} \cdot F_P \right)^{evaporator} + \left(C_{PO} \cdot F_{BM} \cdot F_P \right)^{compressor} + \\ \left(\sum_{i=1}^{I} C_{POi} \cdot F_{BM} \cdot F_P \right)^{flashing} + \left(C_{PO} \cdot F_{BM} \cdot F_P \right)^{preheater} \end{array} \right] \quad (69a)$$

$$CAPEX^{RC} = fac \cdot \left(\frac{CEPCI^{2019}}{CEPCI^{2003}} \right) \cdot \left[\begin{array}{l} \left(C_{PO} \cdot F_{BM} \cdot F_P \right)^{turbine} + \left(C_{PO} \cdot F_{BM} \cdot F_P \right)^{condenser} + \\ \left(C_{PO} \cdot F_{BM} \cdot F_P \right)^{RC\_Pump} \end{array} \right] \quad (69b)$$

$$CAPEX^{STS} = fac \cdot \left(\frac{CEPCI^{2019}}{CEPCI^{2003}} \right) \cdot \left[\begin{array}{l} \left(C_{PO} \cdot F_{BM} \cdot F_P\right)^{boiler} + \left(C_{PO} \cdot F_{BM} \cdot F_P\right)^{SC} + \\ \left(C_{PO} \cdot F_{BM} \cdot F_P\right)^{GFH} + \left(C_{PO} \cdot F_{BM} \cdot F_P\right)^{STS\_Pump} \end{array} \right] \qquad (69c)$$

In the previous formulation, fac represents the annualization factor for the capital investment cost as defined by Smith (2005):

$$fac = \frac{fi \cdot \left(1 + fi\right)^y}{\left(1 + fi\right)^y - 1} \qquad (70)$$

In which, fi indicates the fractional interest rate per year, and y refers to the number of years in the amortization period. In **Eq. (69a) – Eq. (69c)**, C_{PO} represents the basic cost of a unitary equipment (in kUS$) that operates at near-ambient pressure conditions. This unitary cost is obtained from cost correlations as proposed by Turton et al. (2012) and Couper et al. (2010). In addition, F_{BM} is the correction factor of the basic unitary cost, which accounts for the operating pressure and construction materials. Note that the total annualized cost is corrected for the relevant year through the CEPCI index (Chemical Engineering Plant Cost Index).

The operating and maintenance expenses embraces the cost of utilities (*e.g.*, natural gas, cooling water, and electricity), and equipment maintenance as stated as follows.

$$OPEX = \left[\begin{array}{l} \underbrace{C^{CW} \cdot Q^{condenser} + C^{electricity} \cdot \sum_{t \in \mathrm{T}} W_t^{STS\_pump} + C^{NG} \cdot \sum_{t \in \mathrm{T}} Q_t^{GFH}}_{\text{operating expenses}} + \\ \underbrace{0.25 \cdot CAPEX^{RC} + 0.15 \cdot CAPEX^{STS}}_{\text{equipment maintenance}} \end{array} \right] \qquad (71)$$

In which, C^{CW}, $C^{electricity}$, and C^{NG} are cost parameters for cooling water, electricity, and natural gas, respectively. In this study, the maintenance expenses of the Rankine cycle units are considered to be equal to 25% of the corresponding capital costs, while the maintenance expenses of the STS correspond to 15% of the capital costs of the same units.

4.4.2. Environmental Performance Evaluation

The environmental objective function accounts for the environmental impacts associated with utilities consumption, which include electricity (STS pump), natural gas (GFH), and cooling water (condenser). In this study, the environmental impacts are quantified by the LCA-based ReCiPe methodology (Goedkoop et al., 2009). The quantification of environmental impacts is performed by LCA through four key stages. Firstly, the goal and scope are defined. The ReCiPe methodology accounts for 17 different categories of midpoint level impacts that are divided into three main damage groups at end level. Then, the Life Cycle Inventory (LCI) is carried out to appraise all material inputs and outputs, as well as energy inputs and outputs. In the third stage, the Life Cycle Impact Assessment (LCIA) is used to evaluate, weight and quantify the environmental impacts into eco-points. The environmental objective function is expressed by the following equation.

$$EI = LCIA^{electricity} \cdot \sum_{t \in \mathrm{T}} W_t^{STS\_pump} + LCIA^{NG} \cdot \sum_{t \in \mathrm{T}} Q_t^{GFH} + LCIA^{CW} \cdot Q^{condenser} \qquad (72)$$

In which, $LCIA^{electricity}$, $LCIA^{NG}$, and $LCIA^{CW}$ denote the environmental impacts points (eco-points) related to the electricity used by the STS pump, natural gas consumed by the GFH, and cooling water required by the condenser, respectively. The environmental impacts are estimated through total ReCiPe points per year as obtained from the Ecoinvent database (Ecoinvent default, LCIA, ReCiPe Endpoint H/A, Europe/Es). A plant operating time of 8760 h/year is considered to convert original eco-points per energy production units into points per kW year units. The impacts associated with the stage of system construction are neglected as they are usually much smaller than those related to the operation during the system lifetime.

4.5. Optimization Procedure: Epsilon-Constraint Method

The multi-objective NLP problem can be formally expressed as follows.

$$\begin{aligned} &\min \quad \{TAC,\ EI\} \\ &s.t. \quad \text{all equality and inequality constraints} \end{aligned} \tag{73}$$

In which, TAC denotes the total annualized cost as given by **Eq. (68)**, while EI represents the total environmental impact as estimated by **Eq. (72)**. The multi-objective mathematical model was implemented in GAMS software (Rosenthal, 2016) (version 26.1.0), and solved via the epsilon-constraint method (Ehrgott, 2005). The epsilon-constraint method consists of formulating an auxiliary single-objective model, in which one objective is expressed as the main goal whilst the other objective is stated as an additional constraint. Then, the single-objective model is solved several times for different epsilon bound values that are imposed on the problem constraints. This approach allows obtaining a different optimal solution for each of the considered epsilon bound values. Hence, a Pareto curve can be constructed to show the set of alternative solutions, where each solution represents an optimal trade-off between the economic and environmental objective functions (García et al., 2012; Mavrotas, 2009). The local optimizer CONOPT4 was applied to optimize the multi-objective NLP problem with CPU time of ~2 min (180 different time periods and 30 Pareto-optimal solutions).

5. Case Study

An illustrative case study is carried out to assess the effectiveness of the developed approach for the multi-objective optimization of solar-based ZLD desalination systems. The decentralized system is composed of an STS, Rankine cycle unit, and a MEE-MVR desalination plant. **Fig. 1** depicts the schematic diagram for the solar-driven MEE-MVR system as proposed for the ZLD desalination of high-salinity shale gas wastewaters. The treatment capacity of the MEE-MVR desalination plant is equal to 10.42 kg/s of shale gas wastewater. The salt concentration (salinity) of the feed water is considered to be equal to 70 g/kg, and its inlet temperature is 25ºC. For ensuring the ZLD operation, the brine salinity should achieve a minimum value of 300 g/kg (300k ppm) at the system discharge (Han et al., 2017). **Table 1** shows the process and cost parameters used in the mathematical modelling formulation of the zero-liquid discharge MEE-MVR system. Additional data encompass operational limitations on the saturation pressure (200 kPa) and ideal temperature (100ºC) to avoid rusting and fouling-related problems in the evaporator. The latter is a horizontal-tube falling film unit, which is built of nickel. A minimum temperature approach of 2ºC is considered to prevent temperature crossovers in the evaporator effects. Besides, minimum temperature and pressure drops equal to 0.1ºC and 0.1 kPa, respectively, are used between two successive evaporation effects. The maximum compression ratio is limited to 3 in the mechanical vapor compressor (centrifugal/carbon steel), whilst the heat capacity ratio is 1.33 (Onishi et al., 2017a, 2017b, 2017c).

In the STS, solar parabolic trough collectors are considered owing to their greater efficiencies at high temperatures. The thermal fluid is Therminol 72 due to its high thermal stability at temperatures up to 380ºC (Salcedo et al., 2012). The process and cost parameters used for the optimal design of the steam Rankine cycle and STS are presented in **Table 2**. The daily solar irradiance throughout the year in Spain (N 41º7'8'', E 1º14'43'') is displayed in **Table 3**. The minimum temperature difference in the hot end of the condenser is in a range of 5–15°C, while the temperature increase of the thermal fluid in the boiler is 50°C. Cost parameters include prices of electricity (812.47 US$ per kW year), and natural gas (277.03 US$ per kW year), which are retrieved from Eurostat database (2020). The factor of annualized capital cost is equal to 0.163, which corresponds to 10% of interest rate over 10 years of amortization period. **Table 4** presents the environmental impact points of the utilities. The environmental impacts are estimated through total ReCiPe points per year as obtained from the Ecoinvent database. A plant operating time of 8760 h/year is considered to convert original ReCiPe eco-points per energy production units into points per kW year units.

Firstly, the problem is solved by considering each optimization single-objective alone. Thus, the optimization is performed via the minimization of the total annualized cost (TAC), and the total environmental impacts (EI) separately. Note that the minimization of the economic and environmental single-objectives allows obtaining the limits of the epsilon-constraint interval. Then, the latter interval is divided into a set of subintervals and successive optimizations (iterations) are performed through the minimization of the economic objective-function subjected to each environmental upper bound (*i.e.*, epsilon-constraint that ensures that a given environmental limit is not exceeded). By applying the previous epsilon-constraint approach, we obtain a set of optimal trade-off Pareto solutions. The results obtained are discussed as follows.

6. Results and Discussion

6.1. Single-Objective Optimization: EI Minimization

The total annualized cost obtained via the minimization of the environmental objective-function is equal to 45592 kUS$/year, encompassing 45433 kUS$/year associated with capital investment, and 159 kUS$/year related to operating (electricity, natural gas, and cooling water consumption) and maintenance expenses. The capital cost is composed of 2603 kUS$/year for the investment in the MEE-MVR desalination system, and 42830 kUS$/year for the STS and RC units. Also, the total environmental impacts related to utilities consumption (electricity, natural gas, and cooling water) are estimated to be ~193k ReCiPe eco-points/year. This single-objective optimal solution corresponds to the extreme solution referred to as "Design A" in **Fig. 2** and **Fig. 3**. In this case, the solar-based desalination system requires a total area of the solar parabolic trough collectors of $5.2X10^5$ m^2, and the RC steam turbine produces 502.49 kW of electricity to drive mechanical compressor in the MEE-MVR plant.

The optimal MEE-MVR desalination system obtained by the minimization of environmental impacts is composed of two evaporation effects with heat transfers areas of 1268.94 m^2 and 468.64 m^2. In addition, a feeding preheater with a heat transfer area of 100.28 m^2 (1669.63 kW) is required in the system, along with two flashing tanks with volumes of 1.19 m^3 and 2.39 m^3. Note that the capacity of the mechanical vapor compressor is equal to 502.49 kW. Under this configuration, the desalination system achieves a freshwater production ratio of 7.99 kg/s.

6.2. Single-Objective Optimization: TAC Minimization

The total annualized cost obtained via the minimization of the economic objective-function is equal to 2224 kUS$/year, comprising 1794 kUS$/year related to capital investment, and 430 kUS$/year associated with operating (electricity, natural gas, and cooling water consumption) and maintenance expenses. The capital cost is composed of 1166 kUS$/year for the investment in the MEE-MVR desalination system, and 628 kUS$/year for the STS and RC units. Still, the total environmental impacts related to utilities consumption (electricity, natural gas, and cooling water) are estimated to be ~667.5k ReCiPe eco-points/year. This single-objective optimal solution corresponds to the extreme solution referred to as "Design B" in **Fig. 2** and **Fig. 3**. In this case, the solar-based desalination system requires a total area of the solar parabolic trough collectors of 4942 m^2, and the RC steam turbine produces 734.68 kW of electricity to drive mechanical compressor in the MEE-MVR plant.

The optimal MEE-MVR desalination system obtained by the minimization of the total annualized cost is composed of two evaporation effects with heat transfers areas of 284.54 m^2 and 297.22 m^2. In addition, a feeding preheater with a heat transfer area of 68.73 m^2 (1903.66 kW) is required in the system, along with two flashing tanks with volumes of 1.19 m^3 and 2.39 m^3. Note that the capacity of the mechanical vapor compressor is equal to 734.68 kW. Under this configuration, the desalination system achieves a freshwater production ratio of 7.99 kg/s. The comparison between the two extreme environmental and economic optimal solutions reveals that the total heat transfer area of the evaporator is reduced by ~66.5% when the total annualized cost is minimized. Also, the heat transfer area of the feeding preheater is decreased in ~31.5%. Although the compressor capacity is increased in ~46.2%, the minimization of the TAC leads to a reduction of ~55.2% in the capital cost of the MEE-MVR when compared to the minimum EI solution. The capital cost of investment in the STS and RC units is also decreased in ~98.5%, which is mainly due to the reduction of ~99% in the total area of the solar parabolic trough collectors. It should also be noted that the TAC is reduced in ~95.1% while the EI is increased in 245.9%, when contrasting both extreme optimal solutions.

6.3. Multi-Objective Optimization: Pareto Optimal Solutions

The Pareto set of optimal trade-off solutions obtained via the multi-objective optimization procedure are displayed in **Fig. 2**. In this figure, Design A represents the minimum EI solution while Design B indicates the minimum TAC solution. It should be highlighted that each point in the Pareto curve correspond to an optimal system design and associated process operating conditions, which yield a unique combination of environmental and economic performance. Since a given improvement in one criterion can only be attained at the expense of impairing the another one, there is a clear trade-off between environmental and economic objectives. Hence, the minimum EI solution (Design A) shows the worst economic performance whilst the minimum TAC solution leads to the highest environmental impacts. As mentioned before, the TAC of Design A is equal to 45592 kUS$/year, whereas Design B presents a TAC of 2224 kUS$/year. On the other hand, it is also observed an increase in the environmental impacts from ~193k to 667.5k points/year, when moving from Design A to Design B in the Pareto curve.

A thorough examination of **Fig. 2** also reveals that the environmental impacts are significantly reduced by increasing the area of the solar parabolic trough collectors. However, as previously discussed, such EI reduction comes with a considerable increase in the total annualized cost of the system. For further analysis, we solved the model by fixing the solar collector area to zero. In this solution, the TAC of the system is equal to 2243 kUS$/year, whereas the EI are estimated to be 992.3k points/year. The TAC is slightly higher than that of Design B due to the increase in both the capital cost of investment in the MEE-MVR desalination system, and operating expenses related to the larger consumption of natural gas. Clearly, the latter result is also responsible for an increase of ~48.7% in the environmental impacts of the system. Therefore, using solar thermal collectors to drive the MEE-MVR desalination plant is not only an environment-friendly solution but also an economically viable one.

Since Design A and Design B correspond to extreme solutions in the Pareto Curve (which can be prohibitive either in terms of high process costs or excessive environmental impacts), we identify Design C as a promising alternative optimal solution. In this case, the TAC of the system is equal to 6867 kUS$/year, while the total EI related to utilities consumption (electricity, natural gas, and cooling water) is equal to 209.6k ReCiPe eco-points/year. Thus, it is possible to decrease the TAC in ~85% at expense of only 8.5% of increase in environmental impacts when moving from Design A to Design C. The decrease in the TAC is mainly due to the reduction of total area of the solar parabolic trough collectors from 5.2X10^5 m^2 in point A to 4.3X10^4 m^2 in point C. **Fig. 3** shows the dependence of the TAC of the process on the total aperture area of the solar collectors for each optimal design solution. Note that the energy required to drive the MEE-MVR desalination plant is fulfilled using primarily solar collectors in Design A (minimum EI solution). In Design B and Design C, the energy demand is covered by both the GFH and solar collectors. Moreover, the GFH is required in all solutions (even in the minimum EI one) as a result of the solar energy intermittency (particularly in night-time operation).

Fig. 4 and **Fig. 5** depict the solar energy share of each optimal design in different time periods during a day in January and July, respectively. January and July are the months with the lowest and largest daily solar radiation flux (irradiance) in the year, correspondingly. The solar fraction as portrayed in **Fig. 4** and **Fig. 5** corresponds to the amount of energy required by the boiler in the STS that is covered by solar collectors. In January, all energy demands of Design A (minimum EI solution) are completely fulfilled by solar collectors in time periods ranging from 7 to 17h. This is due to the large area of the solar collectors used in this optimal solution. As a consequence of the highest solar irradiance in July, the time periods in which all energy requirements of Design A are covered by solar collectors are extended from 5 to 18h. Similar behaviors are observed for Design C in the winter and summer days. However, Design C only requires 17.9% of solar fraction in the time period 5-6h because of its low solar irradiance (and smaller solar collectors' area). Note that in remaining hours of the day, the desalination systems of Design A and Design C are completely operated by using natural gas in the GFH. Since the solar collector area is significantly smaller in Design B (minimum TAC solution), the solar energy shares are considerably reduced in this solution. For instance, 82.3% of energy requirements of Design B in January are fulfilled by solar collectors in peak solar irradiance periods (11-13h). Design B only achieves 100% of solar fraction share in the peak solar irradiance periods of July. Therefore, better advantage can be taken from the available solar irradiance by increasing the collectors' area.

Fig. 6 exhibits the costs breakdown for the different optimal design solutions. The TAC of the Design C (6867 kUS$/year) is comprised by 6721 kUS$/year associated with capital investment in equipment, along with 146 kUS$/year related to operating (electricity, natural gas, and cooling water consumption) and maintenance expenses. As the MEE-MVR desalination plant of Design C is similar to that obtained in Design A, both solutions present the same corresponding capital cost of investment (2603 kUS$/year). However, the capital cost of investment in the STS is decreased by 90.4% as a result of the much smaller solar collectors required in Design C. The environmental impacts breakdown for the different design solutions are displayed in **Fig. 7**. As expected, Design B shows the highest environmental impacts related to natural gas consumption (~662k ReCiPe eco-points/year). The environmental impacts of natural gas usage in Design B are ~71.4% higher than those in Design A.

Fig. 8 and **Fig. 9** display the thermal power share in different time periods in January and July, respectively. As shown in **Fig. 8 (a)**, the energy demands of the boiler in Design B are covered by both the GFH and solar collectors in the time periods ranging from 7 to 17h, while the corresponding energy requirements are completely fulfilled by solar collectors in Design C. A similar behaviour is observed for Design B and Design C in time periods ranging from 6 to 18h of a day in July (**Fig. 9 (a)** and **Fig. 9 (b)**, respectively). This is a result of the greater solar collector's area required by solution C. Hence, even in the months of lower solar irradiance, the energy performance of the system can be improved by increasing the collectors' area. Although the latter can represent an increase in the capital costs of the STS (84.7%), the natural gas consumption can be significantly reduced as well as its corresponding environmental impacts (68.9%). Noticeably, other alternative trade-off optimal solutions can be chosen in the Pareto curve to reduce the capital costs required for solar collectors at expense of small increases in environmental impacts. For that reason, the Pareto curve obtained can be a useful tool for decision-makers towards the implementation of cost-effective and environment-friendly desalination systems according to their preferences.

7. Conclusions

A new multi-objective model is developed for the thermo-economic and environmental optimization of solar-driven ZLD systems, which are particularly applied to the desalination of high-salinity shale gas wastewaters. A decentralized ZLD system is proposed encompassing a solar thermal-assisted Rankine cycle unit coupled to a MEE-MVR desalination plant. The solar thermal system is designed for multi-period operation according the daily solar irradiance throughout the year. Also, the ZLD operation of the desalination plant is ensured by specifying the discharge brine salinity close to salt saturation conditions. The resulting multi-objective NLP model is implemented in GAMS and solved by the epsilon-constraint method via the minimization of the TAC and environmental impacts. The economic objective function accounts for the capital cost of investment in equipment, along with maintenance and operating expenses related to utilities consumption. The environmental performance is assessed by the LCA-based ReCiPe methodology.

A case study based on Spain's weather conditions is performed to demonstrate the applicability of the proposed multi-objective approach. A set of trade-off Pareto solutions is obtained revealing a reduction of ~95.1% in the TAC at the expense of increasing environmental impacts in 245.9%, when comparing minimum economic and environmental optimal solutions. The Pareto curve also shows that intermediate optimal solutions provide significant reductions in environmental impacts at small increases in the total costs. The environmental impacts are mainly decreased by enlarging the area of the solar parabolic trough collectors, which reduces the natural gas consumption and leads to savings in operating expenses. Hence, the use of solar thermal collectors to operate the

MEE-MVR desalination system can be not only an eco-friendly alternative but also a cost-effectively solution. Thus, our comprehensive multi-objective approach represents a useful tool able to identify the best alternatives that simultaneous balance both environmental and economic criteria. For this reason, our multi-objective model can be used to support the decision-making process towards implementing more sustainable and cost-efficient solar-driven ZLD desalination systems.

Acknowledgements

This project has received funding from the European Union’s Horizon 2020 Research and Innovation Programme under grant agreement No. 640979.

Nomenclature

Acronyms

BPE	Boiling Point Elevation
CEPCI	Chemical Engineering Plant Cost Index
CSP	Concentrated Solar Power
GAMS	General Algebraic Modelling System
GHF	Gas-fired Heater
LCA	Life Cycle Assessment
LCI	Life Cycle Inventory
LCIA	Life Cycle Impact Assessment
MD	Membrane Distillation
MEE	Multiple-Effect Evaporation
MED	Multiple-Effect Distillation
MVR	Mechanical Vapor Recompression
MSF	Multistage Flash Distillation
NEA	Non-Equilibrium Allowance
NLP	Non-linear Programming
RC	Rankine Cycle
RO	Reverse Osmosis
STS	Solar Thermal System
ZLD	Zero-Liquid Discharge

Roman letters

A	Heat transfer area, m^2
BPE	Boiling point elevation, ºC
C^{CW}	Parameter for cooling water cost, US$/kW year
$C^{electricity}$	Parameter for electricity cost, US$/kW year
C^{NG}	Parameter for natural gas cost, US$/kW year
$CAPEX$	Capital Expenditures, kUS$/year

Cp	Specific heat, kJ/kg ºC
C_{PO}	Cost of equipment unit, kUS$
$CR_{\max}$	Maximum compression ratio
EI	Total environmental impact, points/year
fac	Factor of annualized capital cost
F_{BM}	Correction factor for the capital cost
fi	Fractional interest rate per year
F_P	Parameter for the capital cost estimation
G	Solar radiation flux (irradiance), kW/m^2
H	Specific enthalpy, kJ/kg
$LCIA$	Environmental impacts points, points/kW year
LHV	Lower heating value
L_{MTD}	Logarithmic mean temperature difference
$\dot{m}$	Mass flowrate, kg/s
$OPEX$	Operational Expenses, kUS$/year
P	Pressure, kPa
$\Delta P_{\min}$	Minimum pressure approach, kPa
Q	Heat flow, kW
rt	Retention time in the flashing tanks, min
S	Salinity, g/kg
s	Specific entropy, kJ/kg
T	Temperature, ºC
TAC	Total annualized cost, kUS$/year
$\Delta T_{\min}$	Minimum temperature approach, ºC
U	Overall heat transfer coefficient, kW/m^2 K
V	Volume, m^3
X^{salt}	Salt mass fraction
x	Vapor quality

W	Compression work, kW
y	Number of years

Subscripts

i	Evaporation effects
in	Inlet condition
out	Outlet condition
t	Time period

Superscript

amb	Ambient
avg	Average
cv	Condensate (or Distillate) vapor
CW	Cooling water
GFH	Gas-fired heater
IS	Isentropic
L	Liquid
mix	Mixture
ng	Natural gas
RC	Rankine Cycle
sat	Saturated vapor
SC	Solar collectors
STS	Solar thermal system
sup	Superheated vapor
V	Vapor

Greek letters

γ	Heat capacity ratio
η	Efficiency

θ	Temperatures difference, ºC
λ	Latent heat of vaporization, kJ/kg
ν	Specific volume
ρ	Density, kg/m^3

References

Aboelmaaref, M.M., Zayed, M.E., Zhao, J., Li, W., Askalany, A.A., Salem Ahmed, M., Ali, E.S., 2020. Hybrid solar desalination systems driven by parabolic trough and parabolic dish CSP technologies: Technology categorization, thermodynamic performance and economical assessment. Energy Convers. Manag. 220, 113103. https://doi.org/10.1016/j.enconman.2020.113103.

Acharya, H.R., Henderson, C., Matis, H., Kommepalli, H., Moore, B., Wang, H., 2011. Cost effective recovery of low-TDS frac flowback water for re-use. Glob. Res. 1–100.

Al-Mutaz, I.S., Wazeer, I., 2014. Comparative performance evaluation of conventional multi-effect evaporation desalination processes. Appl. Therm. Eng. 73, 1194–1203. https://doi.org/10.1016/j.applthermaleng.2014.09.025.

Chen, J.J.J., 1987. Comments on improvements on a replacement for the logarithmic mean. Chem. Eng. Sci. 42, 2488–2489. https://doi.org/10.1016/0009-2509(87)80128-8.

Couper, J.R., Penney, W.C., Fair, J.R., Walas, S.M., 2010. Chemical Process Equipment, Selection and Design, second ed. Elsevier, USA.

Ehrgott, M., 2005. Multicriteria optimization. Springer Verlag, New York.

EIA, 2016. U.S. Energy Information Administration. How much carbon dioxide is produced per kilowatthour when generating electricity with fossil fuels?

European Commission, 2016. Eurostat.

García, N., Ruiz-Femenia, R., Caballero, J.A., 2012. Teaching mathematical modeling software for multiobjective optimization in chemical engineering courses. Educ. Chem. Eng. 7, e169–e180. https://doi.org/10.1016/j.ece.2012.07.001.

Ghenai, C., Kabakebji, D., Douba, I., Yassin, A., 2021. Performance analysis and optimization of hybrid multi-effect distillation adsorption desalination system powered with solar thermal energy for high salinity sea water. Energy 215, 119212. https://doi.org/10.1016/j.energy.2020.119212.

Goedkoop, M., Heijungs, R., Huijbregts, M., Schryver, A. De, Struijs, J., Zelm, R. Van, 2009. ReCiPe 2008. Potentials 1–44.

Han, D., He, W.F., Yue, C., Pu, W.H., 2017. Study on desalination of zero-emission system based on mechanical vapor compression. Appl. Energy 185, 1490–1496. https://doi.org/10.1016/j.apenergy.2015.12.061.

Karanikola, V., Moore, S.E., Deshmukh, A., Arnold, R.G., Elimelech, M., Sáez, A.E., 2019. Economic performance of membrane distillation configurations in optimal solar thermal desalination systems. Desalination 472, 114164. https://doi.org/10.1016/j.desal.2019.114164.

Kausley, S.B., Malhotra, C.P., Pandit, A.B., 2017. Treatment and reuse of shale gas wastewater: Electrocoagulation system for enhanced removal of organic contamination and scale causing divalent cations. J. Water Process Eng. 16, 149–162. https://doi.org/10.1016/j.jwpe.2016.11.003.

Lemmon, E., McLinden, M., Friend, D. Thermophysical Properties of Fluid Systems, 1980.

Mavrotas, G., 2009. Effective implementation of the ε-constraint method in Multi-Objective Mathematical Programming problems. Appl. Math. Comput. 213, 455–465. https://doi.org/10.1016/j.amc.2009.03.037.

Moore, S.E., Mirchandani, S.D., Karanikola, V., Nenoff, T.M., Arnold, R.G., Eduardo Sáez, A., 2018. Process modeling for economic optimization of a solar driven sweeping gas membrane distillation desalination system. Desalination 437, 108–120. https://doi.org/10.1016/j.desal.2018.03.005.

Najafi, A., Jafarian, A., Darand, J., 2019. Thermo-economic evaluation of a hybrid solar-conventional energy supply in a zero liquid discharge wastewater treatment plant. Energy Convers. Manag. 188, 276–295. https://doi.org/10.1016/j.enconman.2019.03.059.

National Institute of Standards, NIST Chemistry WebBook, 2011.

NRC, 2013. Induced Seismicity Potential in Energy Technologies. National Academies Press, Washington, D.C. https://doi.org/10.17226/13355.

Onishi, V.C., Carrero-Parreño, A., Reyes-Labarta, J.A., Fraga, E.S., Caballero, J.A., 2017a. Desalination of shale gas produced water: A rigorous design approach for zero-liquid discharge evaporation systems. J. Clean. Prod. 140, 1399–1414. https://doi.org/10.1016/j.jclepro.2016.10.012.

Onishi, V.C., Carrero-Parreño, A., Reyes-Labarta, J.A., Ruiz-Femenia, R., Salcedo-Díaz, R., Fraga, E.S., Caballero, J.A., 2017b. Shale gas flowback water desalination: Single vs multiple-effect evaporation with vapor recompression cycle and thermal integration. Desalination 404, 230–248. https://doi.org/10.1016/j.desal.2016.11.003.

Onishi, V.C., Fraga, E.S., Reyes-Labarta, J.A., Caballero, J.A., 2018. Desalination of shale gas wastewater: Thermal and membrane applications for zero-liquid discharge, in: Emerging Technologies for Sustainable Desalination Handbook. Elsevier, pp. 399–431. https://doi.org/10.1016/B978-0-12-815818-0.00012-6.

Onishi, V.C., Reyes-Labarta, J.A., Caballero, J.A., 2019. Membrane Desalination in Shale Gas Industry, in: Current Trends and Future Developments on (Bio-) Membranes. Elsevier, pp. 243–267. https://doi.org/10.1016/B978-0-12-813551-8.00010-3.

Onishi, V.C., Ruiz-Femenia, R., Salcedo-Díaz, R., Carrero-Parreño, A., Reyes-Labarta, J.A., Fraga, E.S., Caballero, J.A., 2017. Process optimization for zero-liquid discharge desalination of shale gas flowback water under uncertainty. J. Clean. Prod. 164, 1219–1238. https://doi.org/10.1016/j.jclepro.2017.06.243.

Pouyfaucon, A.B., García-Rodríguez, L., 2018. Solar thermal-powered desalination: A viable solution for a potential market. Desalination 435, 60–69. https://doi.org/10.1016/j.desal.2017.12.025.

Prpich, G., Coulon, F., Anthony, E.J., 2016. Review of the scientific evidence to support environmental risk assessment of shale gas development in the UK. Sci. Total Environ. 563–564, 731–740. https://doi.org/10.1016/j.scitotenv.2015.11.026.

Richard E. Rosenthal, 2016. GAMS — A User’s Guide. GAMS Development Corporation, Washington, DC.

Salcedo, R., Antipova, E., Boer, D., Jiménez, L., Guillén-Gosálbez, G., 2012. Multi-objective optimization of solar Rankine cycles coupled with reverse osmosis desalination considering economic and life cycle environmental concerns. Desalination 286, 358–371. https://doi.org/10.1016/j.desal.2011.11.050.

Smith, R.M., 2005. Chemical Process Design and Integration. John Wiley & Sons Ltd, England.

Staddon, P.L., Depledge, M.H., 2015. Fracking Cannot Be Reconciled with Climate Change Mitigation Policies. Environ. Sci. Technol. 49, 8269–8270. https://doi.org/10.1021/acs.est.5b02441.

Thomas, M., Partridge, T., Harthorn, B.H., Pidgeon, N., 2017. Deliberating the perceived risks, benefits, and societal implications of shale gas and oil extraction by hydraulic fracturing in the US and UK. Nat. Energy 2, 17054. https://doi.org/10.1038/nenergy.2017.54.

Turton, R., Bailie, R.C., Whiting, W.B., Shaeiwitz, J.A., Bhattacharyya, D., 2012. Analysis, Synthesis, and Design of Chemical Processes, fourth ed.

Zheng, Y., Hatzell, K.B., 2020. Technoeconomic analysis of solar thermal desalination. Desalination 474, 114168. https://doi.org/10.1016/j.desal.2019.114168.

Appendix. Thermodynamic Correlations

The thermodynamic correlations to estimate the boiling point elevation (BPE), and the fluid physical properties are presented as follows.

A.1. Boiling Point Elevation

The BPE corresponds to the raise in the temperature of boiling point triggered by the salt concentration of brine. The BPE in evaporation effect i is estimated by the following equation.

$$BPE_i = \begin{pmatrix} 0.1581 + 2.769 \cdot X_i^{salt} - 0.002676 \cdot T_i^{ideal} \\ + \ 41.78\sqrt{X_i^{salt}} + 0.134 \cdot X_i^{salt} \cdot T_i^{ideal} \end{pmatrix} \quad \forall\, i \in I \qquad \text{(A.1)}$$

Where,

$$X_i^{salt} = 0.001 \cdot S_i^{brine} \quad \forall\ i \in I \qquad \text{(A.2)}$$

In **Eq. (A.1)**, T_i^{ideal} is the ideal temperature ($^{\circ}\mathrm{C}$) and X_i^{salt} the salt mass fraction in the evaporation effect $i \in I$. The ideal temperature is the theoretical temperature that a stream would assume if its salt concentration was equal to zero. In **Eq. (A.2)**, S_i^{brine} is the brine salinity in the effect $i \in I$.

A.2. Physical Properties of Fluids

The thermodynamic properties of fluids in each evaporation effect are estimated via correlations obtained from Aspen HYSYS-OLI. The process simulations have been performed by using the electrolytes thermodynamic package. The thermodynamic correlations for properties estimation are presented as follows. They are valid for temperatures between 10ºC to 120ºC, and salt concentrations in a range of 0 to 0.3.

A.2.1. Specific Enthalpy

The specific enthalpies of liquid and vapor states of fluids in the evaporation effect i are given by the following correlations.

$$H_i^{liquid} = -15940 + 8787 \cdot X_i^{salt} + 3.557 \cdot T_i^{boiling} \quad \forall\ i \in I \tag{A.3}$$

$$H_i^{vapor} = -13470 + 1.840 \cdot T_i^{boiling} \quad \forall\ i \in I \tag{A.4}$$

In which, $T_i^{boiling}$ represents the boiling temperature in effect $i \in I$ given in ºC. To evaluate the specific enthalpies of condensate flows, we consider salt concentrations equal to zero and the corresponding temperature $T_i^{condensate}$ in **Eq. (A.3)**. The specific enthalpy of the feed salt water is also obtained by **Eq. (A.3)** by taking the appropriate salt mass fraction (X_{in}^{feed}) and temperature (T_{in}^{feed}).

A.2.2. Latent Heat of Vaporization

The latent heat of vaporization of the streams in the evaporation effect i is given as follows.

$$\lambda_i = 2502.5 - 2.3648 \cdot T_i^{sat} + 1.840 \cdot \left(T_{i-1}^{sat} - T_i^{sat}\right) \quad \forall\ i > 1 \tag{A.5}$$

In which, T_i^{sat} indicates the temperature of the saturated vapor in effect $i \in I$ expressed in ºC. The saturated vapor temperature is estimated via the Antoine Equation for vapor-liquid equilibrium as shown in **Eq. (A.6)**.

$$\ln\left(P_i^{sat}\right) = A + \frac{B}{\left(T_i^{sat} + C\right)} \quad \forall\ i \in I \tag{A.6}$$

In which, P_i^{sat} is the saturation pressure of streams given in kPa. Moreover, *A*, *B*, and *C* are the Antoine parameters with values equal to 12.98437, -

2001.77468, and 139.61335, correspondingly. **Eq. (A.6)** can also be used to estimate the ideal temperature T_i^{ideal} in evaporation effect $i \in I$. In this case, the pertaining pressure of vapor (P_i^{vapor}) should be considered in **Eq. (A.6)**.

A.2.3. Specific Heat

The specific heat of the feed water in the last evaporation effect $i = I$ is given as follows.

$$Cp_{in}^{feed} = 0.001 \cdot \begin{bmatrix} 4206.8 - 6.6197 \cdot S_{in}^{feed} + 1.2288e^{-2} \cdot \left(S_{in}^{feed}\right)^2 + \\ \left(-1.1262 + 5.418e^{-2} \cdot S_{in}^{feed}\right) \cdot T_{in}^{feed} \end{bmatrix} \tag{A.7}$$

The specific heat of the condensate can be obtained by considering the stream salinity equal to zero in **Eq. (A.7)**. Thus,

$$Cp_i^{condensate} = 0.001 \cdot \left(4206.8 - 1.1262 \cdot T_i^{ideal}\right) \quad \forall\ i = I \tag{A.8}$$

List of Figure Captions

Fig. 1. Schematic diagram for the solar-based zero-liquid discharge desalination system. GFH, gas-fired heater; MEE-MVR, multiple-effect evaporation with mechanical vapor recompression.

Fig. 2. Pareto set of optimal trade-off solutions. Design A indicates the minimum environmental impact solution, while Design B represents the minimum total annualized cost solution.

Fig. 3. Dependence of the total annualized cost of the process on the total aperture area of the solar collectors.

Fig. 4. Solar energy share in different time periods during a winter day in January.

Fig. 5. Solar energy share in different time periods during a summer day in July.

Fig. 6. Breakdown of the total annualized cost for the different design solutions. CAPEXdes, capital cost of the MEE-MVR desalination system; CAPEXsolar, capital cost of the solar thermal system and Rankine cycle units; OPEX, operational and maintenance expenses.

Fig. 7. Breakdown of the environmental impacts for the different design solutions. EI, environmental impacts.

Fig. 8. Thermal power share in different time periods during a winter day in January for (*a*) Design B (minimum total annualized solution); and, (*b*) Design C (intermediate optimal solution).

Fig. 9. Thermal power share in different time periods during a summer day in July for (*a*) Design B (minimum total annualized solution); and, (*b*) Design C (intermediate optimal solution).

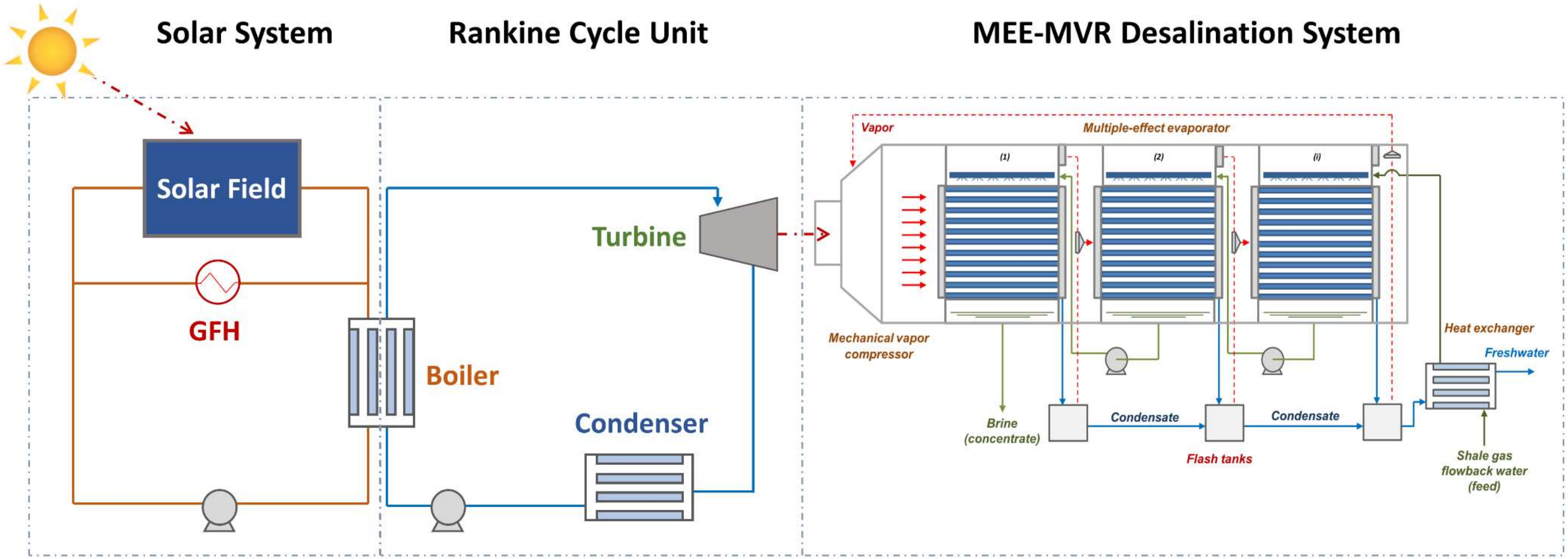

Fig. 1. Schematic diagram for the solar-based zero-liquid discharge desalination system. GFH, gas-fired heater; MEE-MVR, multiple-effect evaporation with mechanical vapor recompression.

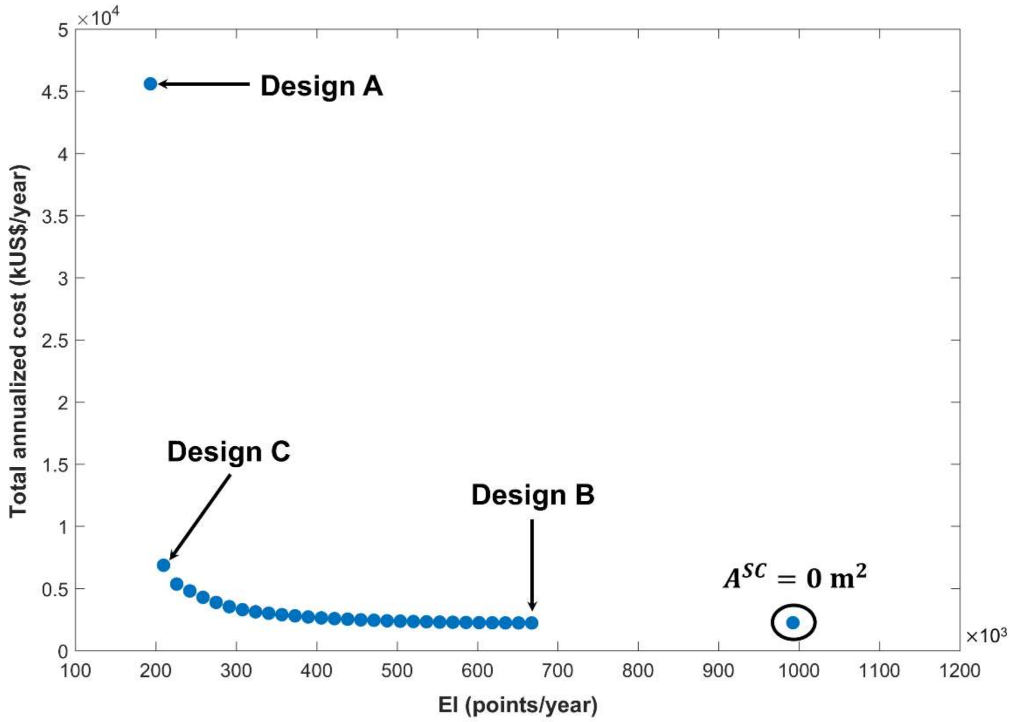

Fig. 2. Pareto set of optimal trade-off solutions. Design A indicates the minimum environmental impact solution, while Design B represents the minimum total annualized cost solution.

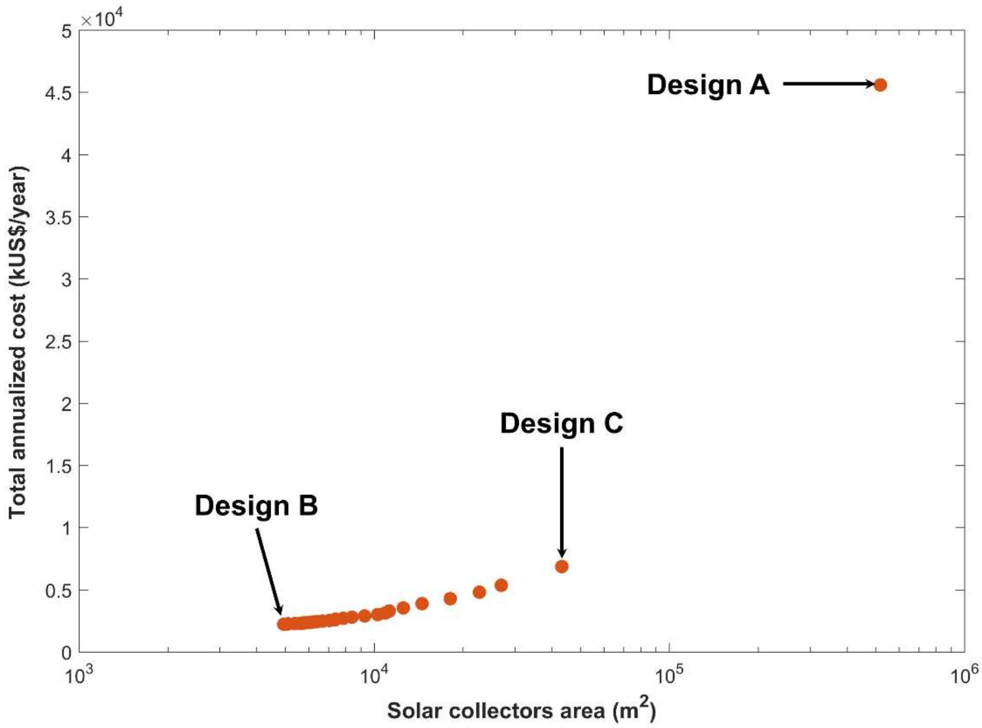

Fig. 3. Dependence of the total annualized cost of the process on the total aperture area of the solar collectors.

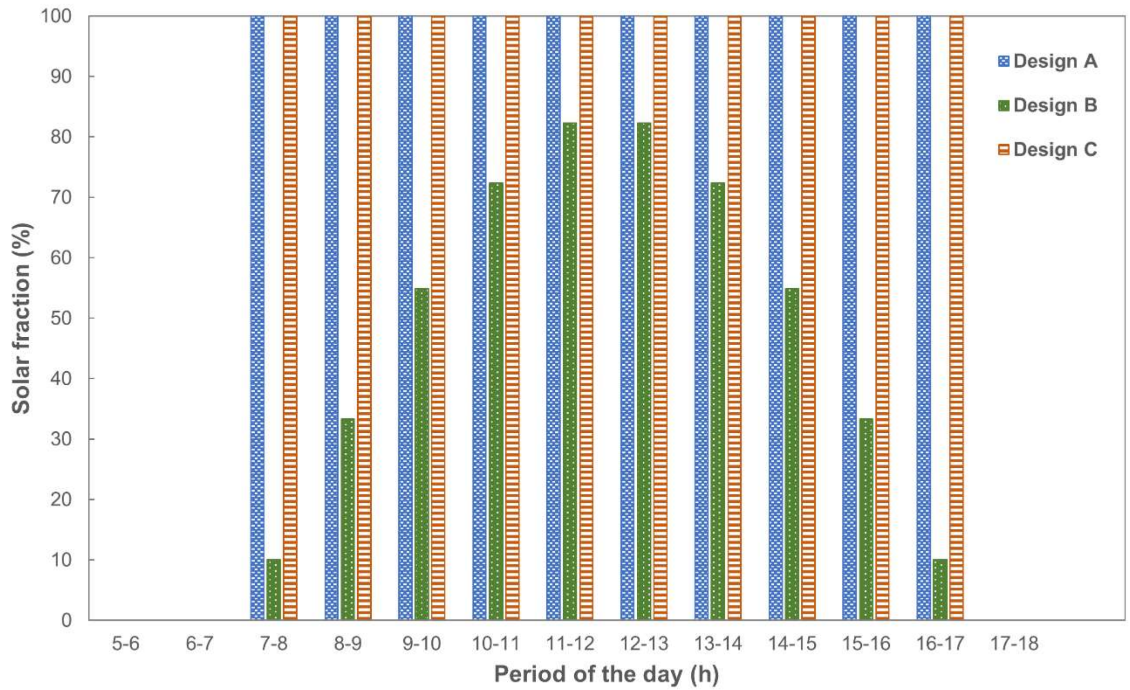

Fig. 4. Solar energy share in different time periods during a winter day in January.

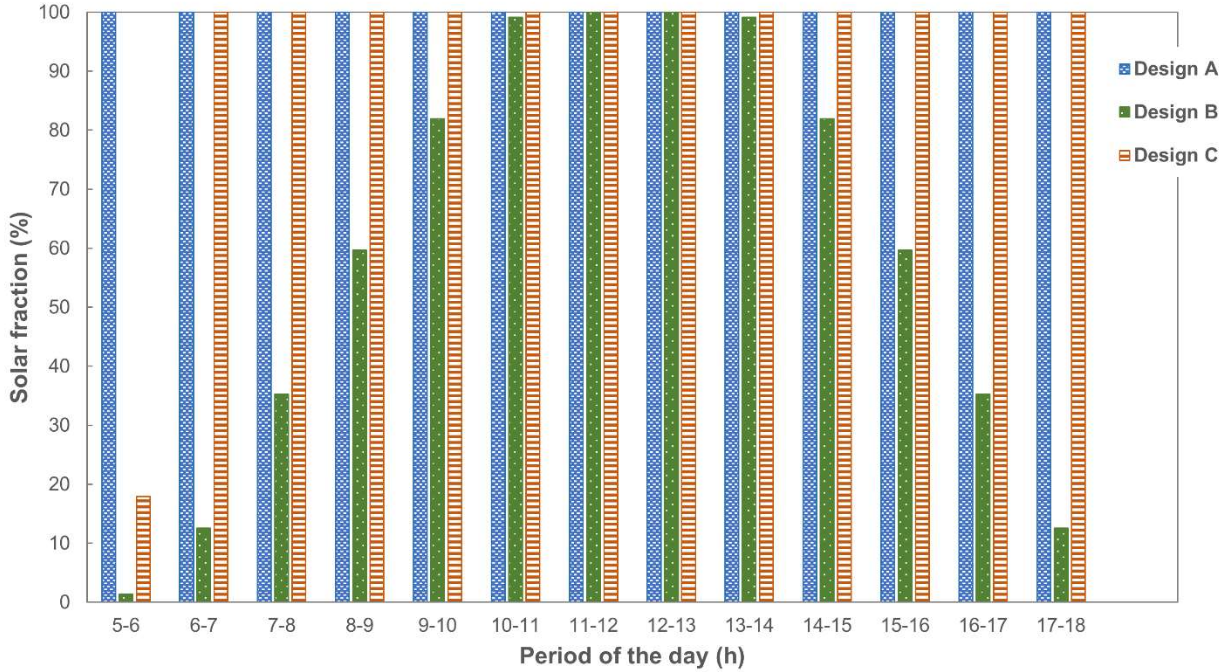

Fig. 5. Solar energy share in different time periods during a summer day in July.

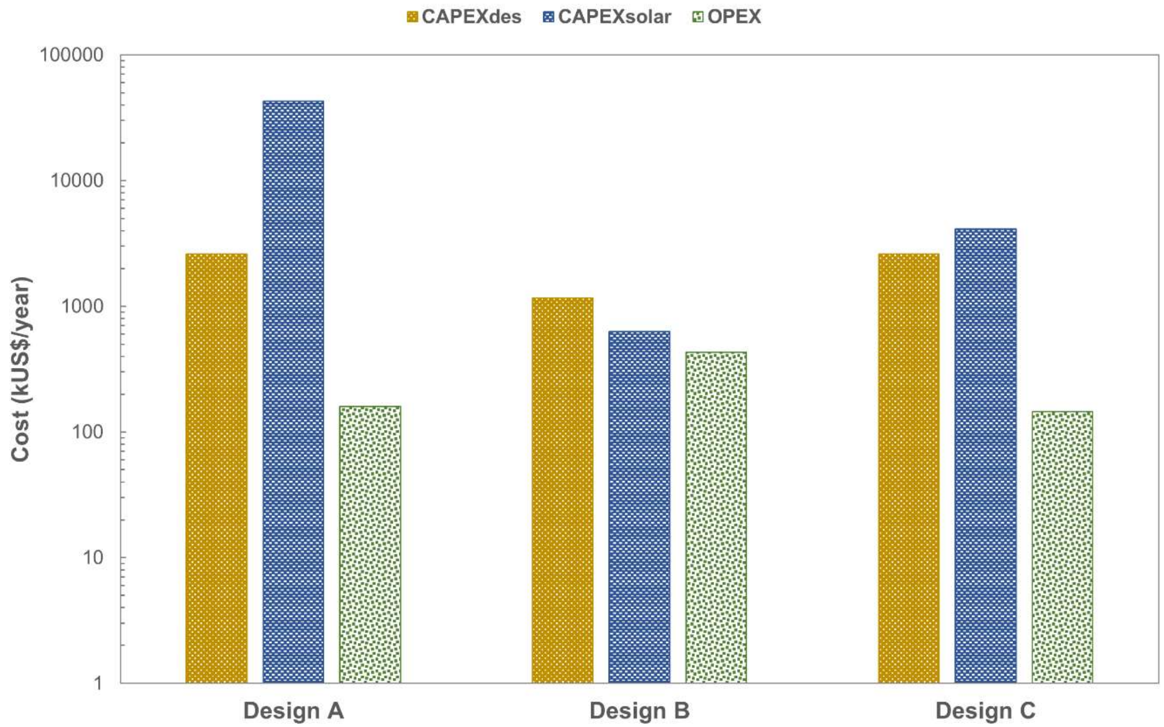

Fig. 6. Breakdown of the total annualized cost for the different design solutions. CAPEXdes, capital cost of the MEE-MVR desalination system; CAPEXsolar, capital cost of the solar thermal system and Rankine cycle units; OPEX, operational and maintenance expenses.

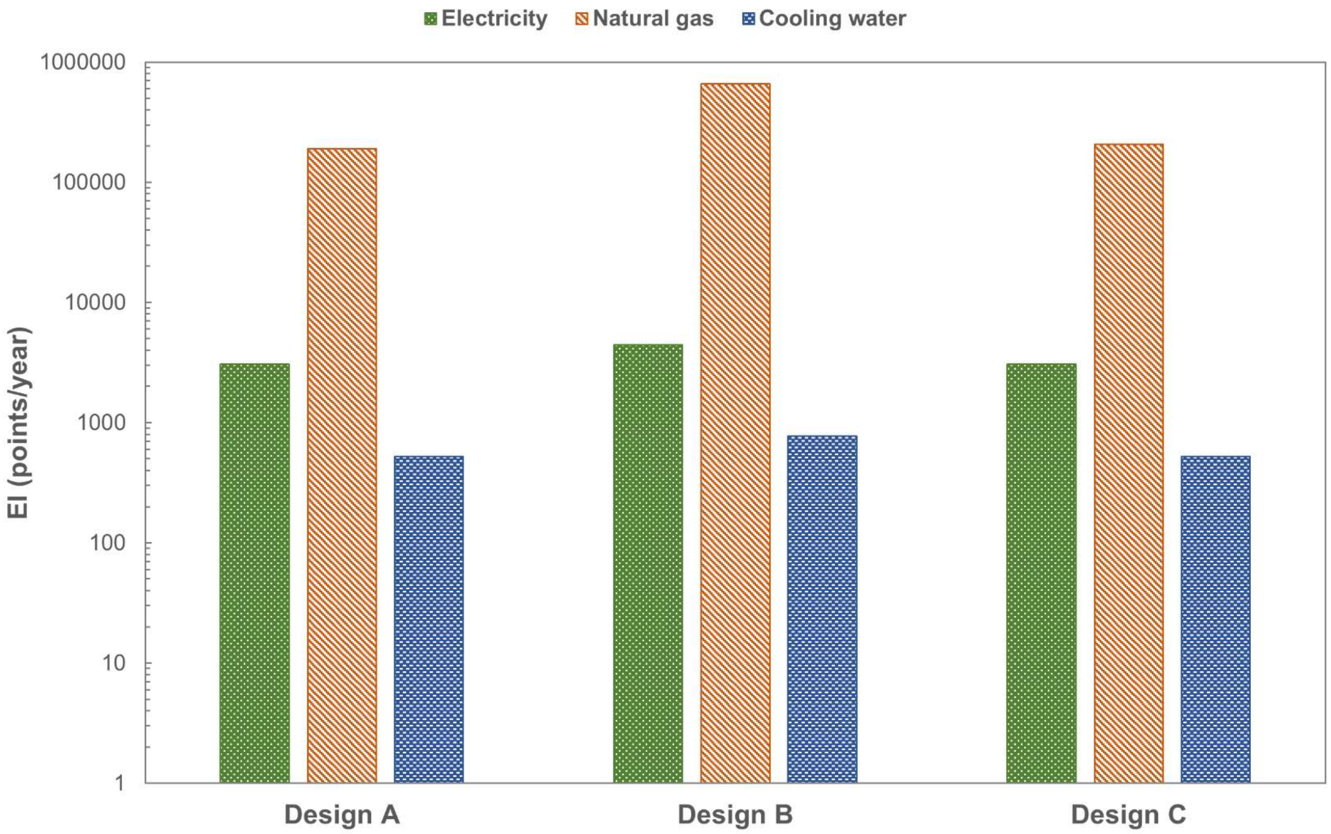

Fig. 7. Breakdown of the environmental impacts for the different design solutions. EI, environmental impacts.

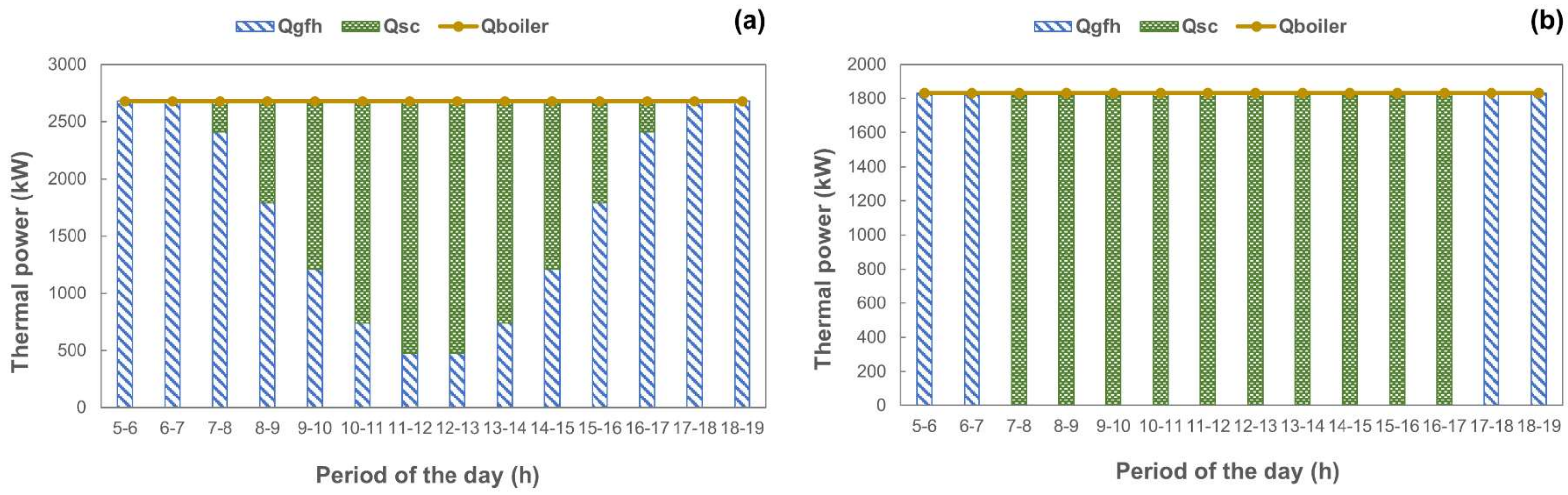

Fig. 8. Thermal power share in different time periods during a winter day in January for (*a*) Design B (minimum total annualized solution); and, (*b*) Design C (intermediate optimal solution).

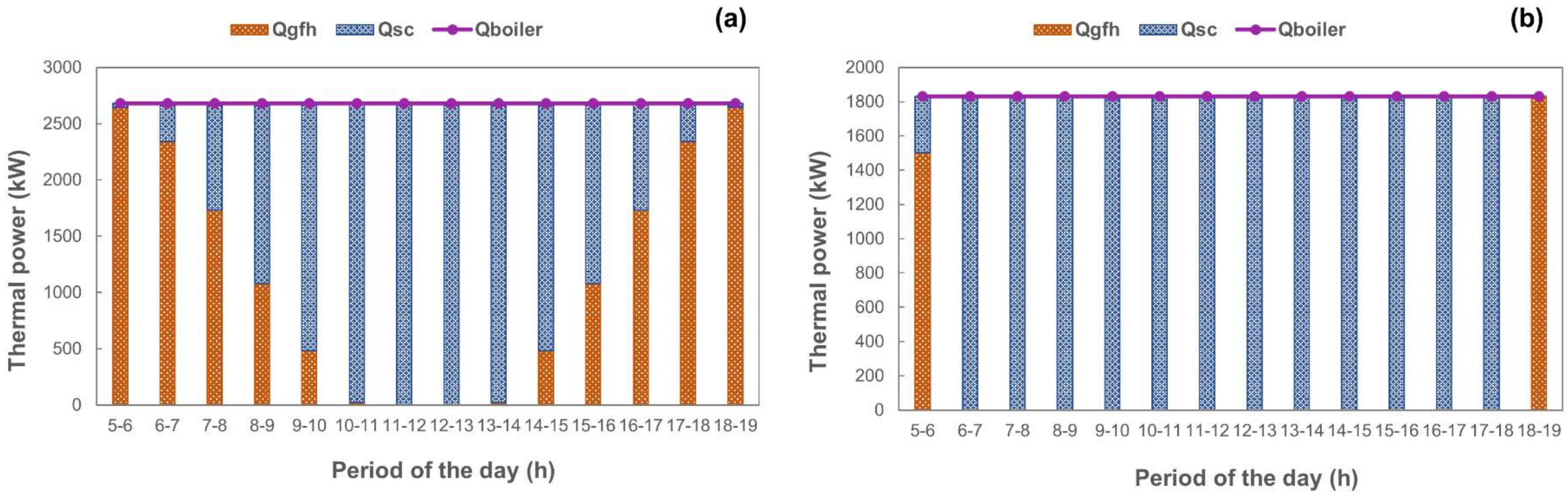

Fig. 9. Thermal power share in different time periods during a summer day in July for (*a*) Design B (minimum total annualized solution); and, (*b*) Design C (intermediate optimal solution).

Table 1

Parameters used in the mathematical model for the optimal design of the zero-liquid discharge MEE-MVR system.

Feed water	Mass flowrate, $\dot{m}_I^{feed}$ (kg/s)	10.42
	Temperature, T_I^{feed} (ºC)	25
	Salinity, $S_{in}^{feed\_water}$ (g/kg or k ppm)	70
Mechanical vapor compressor	Isentropic efficiency, η^{IS} (%)	75
	Heat capacity ratio, γ	1.33
	Maximum compression ratio, $CR_{\max}$	3
Process specification and operating constraints	Salinity of ZLD operation, S^{design} (g/kg or k ppm)	300
	Maximum temperature, T_i^{ideal} (ºC)	100
	Maximum pressure, P_i^{sat} (kPa)	200
	Number of evaporation effects	2
Economic data	Electricity price [1], $C^{electricity}$ (US$/kW year)	812.47
	Fractional interest rate per year, fi	0.1
	Amortization period, y	10
	Working hours per year, (h)	8760

[1] *Cost data obtained from Eurostat database* (2020) *(1st semester – 2020).*

Table 2

Parameters used in the mathematical model for the optimal design of the steam Rankine cycle and solar thermal system (Salcedo et al., 2012).

Rankine cycle	Turbine isentropic efficiency, η^{IS} (%)	78
	Specific heat of water vapor, Cp (kJ/kg K)	2.7
	Inlet cooling water temperature, T_{in}^{CW} (K)	298
	Outlet cooling water temperature, T_{out}^{CW} (K)	308
Solar collectors	Collector optical efficiency, η_0 (%)	75
	Solar collector constant, a_1	4.5e-6
	Solar collector constant, a_2	0.039
	Solar collector constant, a_3	3e-4
	Specific heat of the thermal fluid (Therminol 72), Cp^{hf} (kJ/kg K)	2.528
Gas-fired heater	Efficiency, η^{GFH} (%)	75
	Lower heating value of natural gas, LHV (kJ/kg)	47100
Pump	RC pump efficiency, η^{RC_pump} (%)	60
	Specific volume of working fluid, v (m^3/kg)	1.2e-3
Economic data	Natural gas price [1], C^{NG} (US$/kW year)	277.03
	Fractional interest rate per year, fi	0.1
	Amortization period, y	10
	Working hours per year, (h)	8760

[1] *Cost data obtained from Eurostat database* (2020) *(1st semester – 2020).*

Table 3

Daily solar radiation flux (irradiance)[1] throughout the year (Salcedo et al., 2012).

Month	5-6	6-7	7-8	8-9	9-10	10-11	11-12	12-13	13-14	14-15	15-16	16-17	17-18	18-19
January	0.00	0.00	92.78	260.28	416.67	543.89	615.28	615.28	543.89	416.67	260.28	92.78	0.00	0.00
February	0.00	0.00	155.83	322.22	488.06	621.67	696.39	696.39	621.67	488.06	322.22	155.83	0.00	0.00
March	0.00	57.50	211.11	387.78	559.17	695.56	771.39	771.39	695.56	559.17	387.78	211.11	57.50	0.00
April	3.61	90.00	253.89	433.89	604.44	743.33	816.94	816.94	743.33	604.44	433.89	253.89	90.00	3.61
May	25.28	106.94	272.22	448.06	615.00	741.67	811.11	811.11	741.67	615.00	448.06	272.22	106.94	25.28
June	34.17	112.50	276.94	452.22	611.39	733.61	800.28	800.28	733.61	611.39	452.22	276.94	112.50	34.17
July	30.00	109.44	274.44	450.83	611.94	736.11	803.89	803.89	736.11	611.94	450.83	274.44	109.44	30.00
August	13.89	97.22	261.11	438.61	609.44	740.00	811.39	811.39	740.00	609.44	438.61	261.11	97.22	13.89
September	0.00	70.83	226.67	402.78	571.94	705.83	785.56	785.56	705.83	571.94	402.78	226.67	70.83	0.00
October	0.00	0.00	173.61	341.11	506.67	639.17	713.06	713.06	639.17	506.67	341.11	173.61	0.00	0.00
November	0.00	0.00	112.50	270.56	425.56	551.39	621.94	621.94	551.39	425.56	270.56	112.50	0.00	0.00
December	0.00	0.00	70.28	235.83	386.67	510.00	579.44	579.44	510.00	386.67	235.83	70.28	0.00	0.00

[1] *Irradiance values given in kW/m^2*

Table 4

Environmental impact points of the utilities.

Utility	Process	Total ReCiPe eco-points (points/kW year)
Electricity	Electricity, production mix ES	949.32
Natural gas	Natural gas, burned in industrial furnace >100 kW	454.49
Cooling water	Tap water production, underground water with chemical treatment	0.396